The Hong Kong Polytechnic University

Department of Electronic and Information Engineering

Fabrication and Characterization of Nano/microhole Si Photovoltaic Cells

ZHAO YINGQI

A thesis submitted in partial fulfillment of the requirements
for the Degree of Master of Philosophy

Sept 2011

CERTIFICATE OF ORIGINALITY

I hereby declare that this thesis is my own work and that, to the best of my knowledge and belief, it reproduces no material previously published or written, nor material that has been accepted for the award of any other degree or diploma, except where due acknowledgement has been made in the text.

_____________ (Signed)
ZHAO YINGQI (Name of student)

ABSTRACT

Abstract of thesis entitled ‘Fabrication and Characterization of Micro/nano hole Si Photovoltaic Cells’

Submitted by ZHAO YING QI

Advisers: Prof. CHARLES SURYA

For the degree of Master of Philosophy

At The Hong Kong Polytechnic University in 2011

A simple and cost-effective technique to fabricate wafer-scale silicon nanohole radial p-n junction PVCs has been improved. By combining thermal annealing of Ag thin films and metal catalyzed electroless etching we can fabricate silicon micro/nano holes with controllable size, depth and distribution. We have conducted detailed investigations on the influence of the Ag film thickness, annealing time, annealing temperature, and silicon wafer surface property on the morphology of thermal annealing formed Ag islands. Both P-type Si wafers with both (100) and (111) orientation used in the PVC fabrication. After MCEE the (100) wafers demonstrated lower reflectance, indicating better light trapping property. The PVC with best performance was also based on (100) wafer. The moderate cell performances demonstrate the potential of the technique in large scale fabrication of cost-effective nanostructure PVCs. In addition, the cell performances are investigated in detail as functions of the nanohole dimensions and doping conditions.

ACKNOWLEDGEMENTS

I am honored to have had the opportunity to pursue my Mphil study in the Thin Film Optoelectronics Research Group, PolyU. In particular, I would like to express my sincere thanks to my project advisors Prof. Charles Surya for his guidance and advice, as well as encouragement during my study.

My gratitude goes to the members of Thin Film Optoelectronics Research Group: Dr. Y. Chen, Dr, Kelvin, K. K. Leung, Dr. Patrick, W. K. Fong, Mr. W. Wang, Dr. Hardy, H. F. Liu, Mr. C. W. Lip, for their impairment of knowledge of equipment operation and experimental technique. My thanks are also given to Mr. Z. H. Xu and Mr. J. H. Li from Department of Applied Physics, Mr. J. C. Wang and Ms. Z. R. Wang from Department of Mechanic Engineering for their stimulating discussions, friendship and endless encouragement. Acknowledgements also go to Dr. Y. Y. Li and Ms. L. X. Zheng at City University of Hong Kong (CityU), for their kind assistance in the Si electrochemistry etching process. Besides, my acknowledgements go to Mr. J. A. Huang at CityU for his valuable support in Si nanostructure fabrication. Additionally, I want to thank Prof. H. Shen, Prof. B. Zhang, at Sun Yat-Sen University for their assistance in the device fabrication.

Finally, I deeply thank my family for their countless love, support and understanding throughout the entire period of my studies.

Table of Contents

List of Figures

List of Tables

1 Introduction

1.1 Brief History of Solar Cells

Utilizing solar energy is an effective and promising way to generate energy safely and with little non-desirable environmental impacts. Silicon wafer based solar cells, which is commonly classified as the first generation solar cells, have been commercialized for many years, and still dominate the photovoltaic market, even though the price of refined silicon is relatively high. Although silicon, with indirect band gap, is not an ideal material for solar cells, silicon based solar cells still attract considerable research interests. The main reason is the mature silicon technology provides highly sophisticated processing techniques and availability of high quality materials.

In order to generate electricity at lower cost using solar cells, extensive research efforts have been made to investigate new non-toxic materials with suitable band structure which are cost effective and provide good conversion efficiency. For inorganic materials, thin film copper indium selenide and related chalcopyrites are candidates with great potential, though large scale deployment of the material is quite challenging due to the complexity of the materials [1, 2]. Cadmium telluride, with nearly ideal band structure for single junction solar cell, has also been a potential PV material for solar cell products. Yet Cd and Te are toxic materials, although the compound is stable and harmless[2].

Great effort had been expended within the past decades to develop organic materials based solar cells, which provide the hope of large scale manufacturing at very low cost. However, due to inherent properties of organic PV material, for example poor charge carrier mobility and instability against environmental influence, many improvements need to be made before organic solar cells can be commercialized and practically used[3].

In addition to exploring new materials, other novel concepts of solar cells have been proposed, providing new possibilities for solar energy conversion efficiency improvement. These solar cells include dye-sensitized solar cells[4], solar cells based on auger generation material [5], intermediate metallic band solar cells[6] and so on. Nanotechnology has been investigated for solar cells fabrication. Nanostructures, such as quantum dots, nanowires and nanorods, are incorporated into cell structure, to improve carrier collection, reduce surface reflection, and so on. Nanostructured solar cells, in the recent years, have attracted considerable research interests, since they provide new possibilities of cell performance enhancement and cost reduction.

1.2 Nano-Structured Solar Cells

Utilization of nanostructures may potentially lead to significant reduction in the cost and the efficiency of the solar cells[7]. In the organic and dye-sensitized solar cells nanowires and nanocrystals are used to improve charge collection efficiency[8, 9]. Quantum dots are incorporated into solar cells for carrier multiplication[10]. Among all these concepts, nanowire-based solar cells have attract considerable interests due to their potential advantages in charge collection and light absorption[11].

1.3 Radial p-n junction Solar Cell

In order to solve the trade off between absorption distance and carrier collection length, Kayes proposed in 2005 that Radial PN junction nanorod structure could improve carrier collection by offering long enough absorption distance while maintaining short path for charge collection. In Kayes's paper, it was shown that vertically aligned silicon nanowire solar cells (SNW SCs) are less sensitive to impurities compared to their planar counterparts [12].

Tian and Lieber reported two years later the realization of p-type/intrinsic/n-type(p-i-n) single coaxial silicon nanowire solar cell, the efficiencies of which reached 3.4%[7]. Since then many attempts have been made to fabricate SNW SCs with radial PN junction, using various fabrication approaches to lower cost while improve efficiency[13, 14]. Silicon nanowire-based solar cells on metal foil are reported by Tsakalakos [15], who also investigated the optical reflectance reduction of silicon nanowires film [16]. Garnett, reported in 2008 that fabrication of wafer-scale arrays of n-type Si using metal assist solution phase etching and the deposition of p-type amorphous silicon with low pressure chemical vapor deposition (LPCVD). The efficiency of the solar cell was only about 0.5%[17].

Recently, Garnett reported the fabrication and characterization of solar cells with large scale ordered SNW array, the efficiency of which is about 5%. The fabrication process includes using deep reactive ion etching (RIE) to etch the silicon wafer, the utilization of silica nano-spheres monolayer on the surface as an etch mask, and gas phase diffusion to form p-n junction[18]. In addition, light trapping using silicon nanowire array was also investigated experimentally indicating unique light absorbing property of SNW array.

Silicon nanohole solar cells with radial p-n junction formed by thermal dopant diffusion was reported by Peng and Wang [19]. Deep ultraviolet lithography (UVL) and metal enhanced silicon etching were combined to synthesize wafer-scale nanohole array. The efficiency of this new geometry solar cell reaches 9.51%. As to the fabrication approaches, deep UVL can yield wafer scale ordered silicon nanohole array, yet the resolution of nanohole pattern is limited. What's more, deep UVL equipment is not quite commonly available.

More recently, SiNW radial junction solar cells have demonstrate high values of η of ~10.8% using self-powered parallel electron lithography and radioactive β-electron film emitters[20]. However, all these techniques involved the use of expensive equipment and processes, such as e-beam lithography and deep UVL, which added significantly to the cost of the Solar Cells.

Though nanowire solar cells have advantages in carrier collection and light trapping, surface recombination, which is inherent from large surface area of nanostructures lowers the open circuit voltages and efficiencies of solar cells. With the possibility of striking a balance between light absorption and surface recombination, micro-wire solar cells have also drawn significant research interests. Among all the researchers, Atwater's group have conducted extensive studies on the fabrication of SCs based on Si micro-wire, and 9% conversion efficiency has been achieved[21]. However, additional light trapping materials, for example Al_2O_3 nanoparticles, need to be added to enhance light absorption, due to weaker light trapping in micro-wires arrays comparing with wire arrays with sub-wavelength diameters. By peeling the wire array from the substrate in a flexible polymer and to reuse the growth substrate, they demonstrated the possibility of fabricating flexible high efficiency c-Si SCs[22, 23]. Although, at the present stage, the cell efficiencies of nanostuctured Si based PVCs are much lower than commercialized single crystalline Si PVCs, due to the high surface recombination velocities, of the nanostructures with large surface area, as well as unoptimized fabrication technique, they are considered to possess significant potential the development of light weight and high efficiency PVCs once an effective passivation process is developed to minimize the impact of the surface states.

1.4 Motivation and Thesis Overview

In order to strike a balance between the cost and controllability, we fabricate radial p-n junction solar cells based on random silicon nanohole. By combining metal film thermal annealing and metal catalyzed silicon etching (MCEE) silicon nanoholes with controllable size and inter-hole distance can be fabricated. To have a better control of the hole size distribution and inter-hole distance, the influences of silver thickness, annealing temperature, annealing time, and the recipe of etching solution on the morphology of generated nanohole are examined.

Systematic investigations on the influences of the nanohole dimension and doping conditions on the cell performances were performed to further explore the potential of this random hole system for cost effective PVC fabrication. Our data indicate substantial improvements in the cell efficiency, η, for the devices compared to reported values for random nanostructure PVCs through systematic optimization of the nanohole dimension and doping conditions.

To further lower the fabrication cost, utilization Cu to catalyze Si etching was investigated using an electrochemistry cell and performed under voltage bias. Though current results show the possibility of this method, more detailed investigations and explorations are still needed to apply this method for PVC fabrication.

The thesis is organized as follows: Chapter 2 introduces the basic theory of solar cells and radial p-n junction solar cells, silicon nanostructure fabrication technique and frequently used characterization methods. Chapter 3 presents detailed experimental processes of three parts: 1. Ag film thermal annealing; 2. Ag catalyzed silicon electrodeless electrochemistry etching & Cu catalyzed electrochemistry etching of Si; 3.solar cell fabrication. Chapter 4 shows the experimental results, discusses and analyzes them in three parts corresponding to the arrangement in chapter 3. Finally, chapter 5 summarizes the issues presented in the thesis, represent the directions for future work.

2 Theoretical Overview of Photovoltaic Cells and Characterization Techniques

2.1 Basic principle of conventional PVC

A photovoltaic cell is a solid state electronic device that converts solar energy into electricity via photovoltaic effect, which indicate the generation of electricity current upon exposure to light[24]. When the sunlight incident onto the semiconductor material, electrons and holes are excited by the photons, then separated by the built-in field at the p-n junction. Electrons and holes are collected in n-type and p-type regions separately, and resulting in the current and voltage generation across the junction. Figure 2.1 below illustrates a basic crystalline Si photovoltaic cell. In this section, the basic theory and physics of photovoltaic cell operation and carrier recombination mechanisms are reviewed.

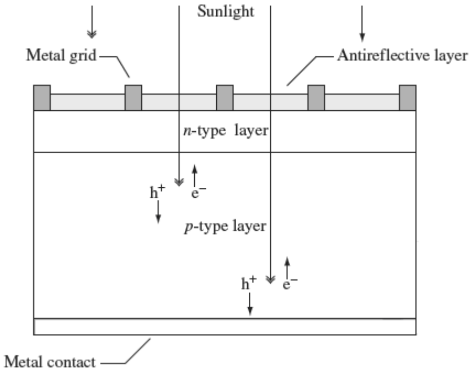

Figure 2.1 : A schematic of a simple conventional photovoltaic cell.[25]

2.1.1 Light Absorption

In this section, the photon interactions with materials that give rise to absorption will be briefly examined. Figure 2.2 shows various processes of electromagnetic radiation absorption in solids and their influencing range, as listed below[25, 26]:

1. Intra-band transition absorption – It arises from photon-induced, electron (or hole) transitions within a band.
2. Phonon absorption – Phonon modes are excited by light absorption in material. Such process occurs in the infrared region of light spectrum due to its low energy property.
3. Localized state absorption – It includes all the photon excited transitions between gap states, as well as between gap states and a band.
4. Exciton-producing absorption – Generally this process occurs in organic absorb materials, such as small-molecule dyes and polymer absorbers.
5. Inter-band transition absorption – This is the main process in crystalline Si photovoltaic cells creating electron-hole pairs and contribute to the electricity generation.
6. Hopping – It is a loss observed in some amorphous materials.

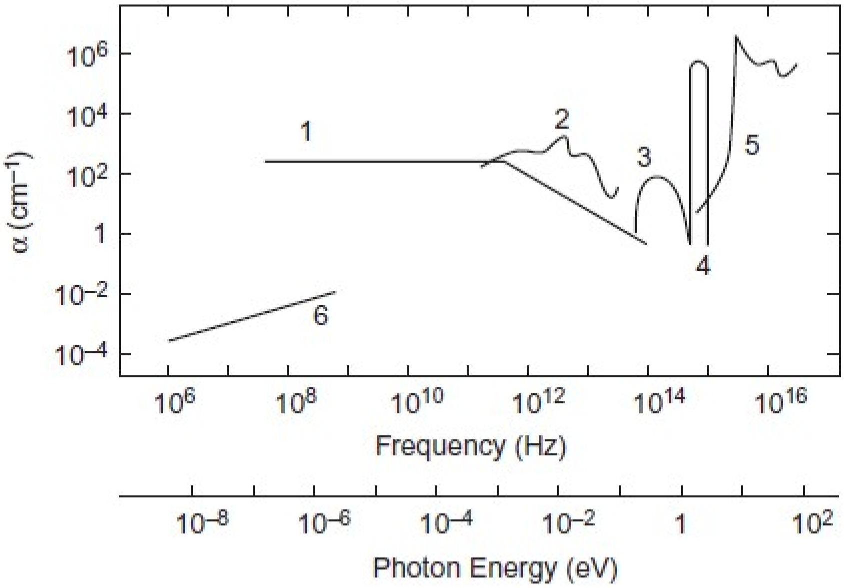

Figure 2.2**:** A schematic portrayal of the range of optical absorption processes in solids.[26]

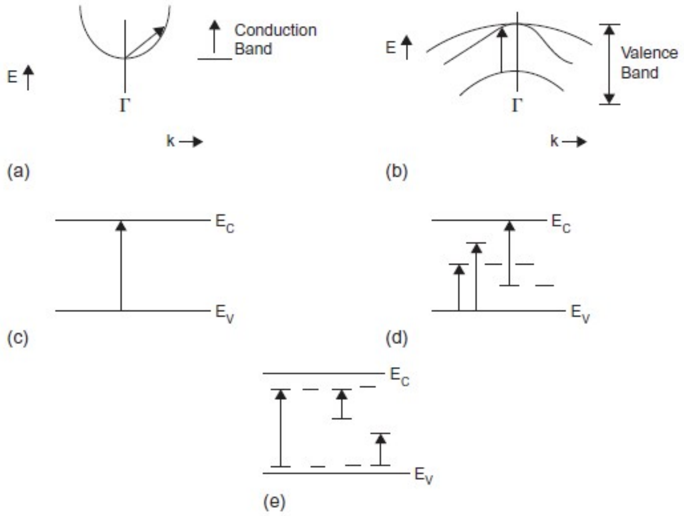

Figure 2.3: Electron transitions between single-electron states that give rise to light absorption: (a, b) free-carrier (intraband) transitions give rise to Process 1 of Figure 2.2 ;(c) band-to-band transitions give rise to Process 5; (d, e) band-localized– state transitions and localized-state – localized-state transitions are the source of Process 3. The type of Process 3 seen in (d) can give rise to free carriers.[26]

The creation of light excited electron–hole pair is fundamental to the operation of photovoltaic cells. The inter-band transition absorption (process 5 in figure 2.2) which excite an electron directly from the valence band to the conduction band is called fundamental absorption.[25 26]

The absorption coefficient α (λ) (equivalently α (hν)), which is the y axis in Figure 2.1 , is an important parameter that quantifies absorption of photons in the material. The absorption coefficient, α (hν), for a given photon energy, hν, is proportional to: 1.) the probability of the transition of an electron from the initial state E1 to the final state E2; 2.) the density of electrons in the initial state; and 3.) the density of available final states. [25, 26]

In direct band gap semiconductors, the basic inter-band transition process is illustrated in Figure 2.4. Both energy and momentum are conserved in the transition. In indirect band gap semiconductors like Si and Ge, there is a difference in the crystal momentum between valence-band (VB) maximum and conduction-band minimum CB. Since conservation of electron momentum necessitates, the photon absorption (process 3 in figure 2.2) involves an additional particle: phonons, which are low-energy particles with relatively high momentum, illustrated in figure 2.5. Since a phonon and an electron are involved in the absorption, the absorption coefficient is determined not only by the density of the initial and final electron states, but also by the availability of phonons with the required momentum. Therefore, generally the absorption coefficients of indirect band gap materials are smaller than direct band materials[25].

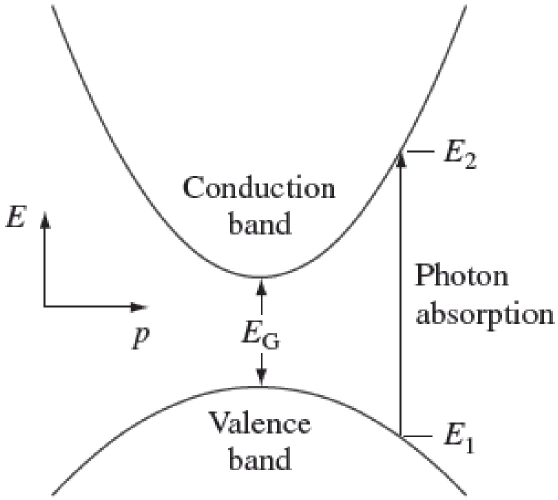

Figure 2.4: Photon absorption in a direct band gap semiconductor for an incident photon with energy $hv = E_2 - E_1 > E_G$[25]

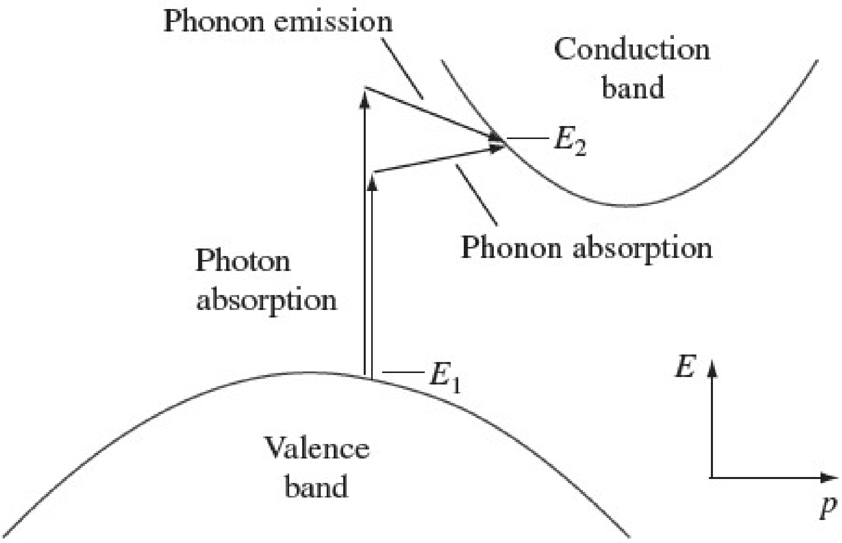

Figure 2.5: Photon absorption in an indirect band gap semiconductor for a photon with energy $h\nu < E2 - E1$ and a photon with energy $h\nu > E2 - E1$. Energy and momentum in each case are conserved by the absorption and emission of a phonon respectively.[25]

The rate of electron–hole pair generation (number of e-h pairs per cm^3 per second) as a function of position within photovoltaic cells is:

$$G(x) = (1-s)\int_{\lambda} (1-r(\lambda))f(\lambda)\alpha(\lambda)e^{-\alpha x}d\lambda \tag{2. 1}$$

Where s is the grid-shadowing factor, $r(\lambda)$ is the reflectance, $\alpha(\lambda)$ is the absorption coefficient, $f(\lambda)$ is the incident photon flux, and the sunlight is assumed to be incident at $x = 0$.[25]

2.1.2 Recombination

The created electrons and holes tend to relax back toward their equilibrium states or drop in energy into some gap state through recombination process, without contributing to the electricity generation. There are several recombination mechanisms:

1. Radiative recombination – an electron can give up its energy through emission of a photon;
2. Shockley-Read-Hall or gap-state-assisted recombination – electron loses energy by emission of phonons and recombination by a localized state in the band gap;
3. Auger recombination –an electron gives up its energy by an Auger mechanism, which involves the transfer of energy to another electron or hole.

Radiative recombination is the inverse of inter-band transition absorption. While the electron loses its energy, a photon will be emitted in direct band semiconductor, and both photon and phonon will be emitted in indirect band semiconductor. The net recombination rate due to radiative processes in p-type material is given as[26]:

$$R^R = \frac{n - n_0}{\tau_n^R} \tag{2. 2}$$

where τ_n^R is the called the electron radiative recombination lifetime or electron lifetime, The dimensions of R^R are number of recombination per volume per time.

Similarly, in n-type materials, recombination is expressed as:

$$R^R = \frac{p - p_0}{\tau_p^R} \tag{2. 3}$$

where τ_p^R is the hole radiatieve recombination lifetime or hole lifetime.

In Shockley-Read-Hall recombination, charge carriers can give up their energy by collisions with the physical entities that gives rise to gap status, and then trapped by them. The energy may be given to phonons or photons or both. The net recombination rate of Shockley-Read-Hall in p-type material is[26]:

$$R^L = \frac{n - n_0}{\tau_n^L} \tag{2. 4}$$

where τ_n^L is the electron S-R-H recombination lifetime or electron lifetime. In n-type materials the net S-R-H recombination is:

$$R^L = \frac{p - p_0}{\tau_p^L} \tag{2. 5}$$

where τ_p^L is the hole S-R-H recombination lifetime or hole lifetime.

Auger recombination resembles radiative recombination, except that the lost energy of the electron is transferred to another carrier, which then releases its excess energy and momentum to phonons. There are many possible types of Auger processes, some of them are shown in figure 2.6[5, 25]. Often Auger recombination in p-type materials can be adequately represented by a linearized model:

$$R^A = \frac{n - n_0}{\tau_n^A} \tag{2. 6}$$

where τ_n^A is the electron Auger recombination lifetime or electron lifetime. In n-type materials the net Auger recombination is:

$$R^A = \frac{p - p_0}{\tau_p^A} \tag{2. 7}$$

On the interface of photovoltaic cells, such as the front surface, high concentration defect occurs, and act as recombination centers. The rate of surface recombination in p-type is written as[25, 27]:

$$R^S = S_n \left(n - n_0 \right) \tag{2. 8}$$

and in n-type materials as:

$$R^S = S_p \left(p - p_0 \right) \tag{2. 9}$$

S_n and S_p are effective surface recombination velocities.

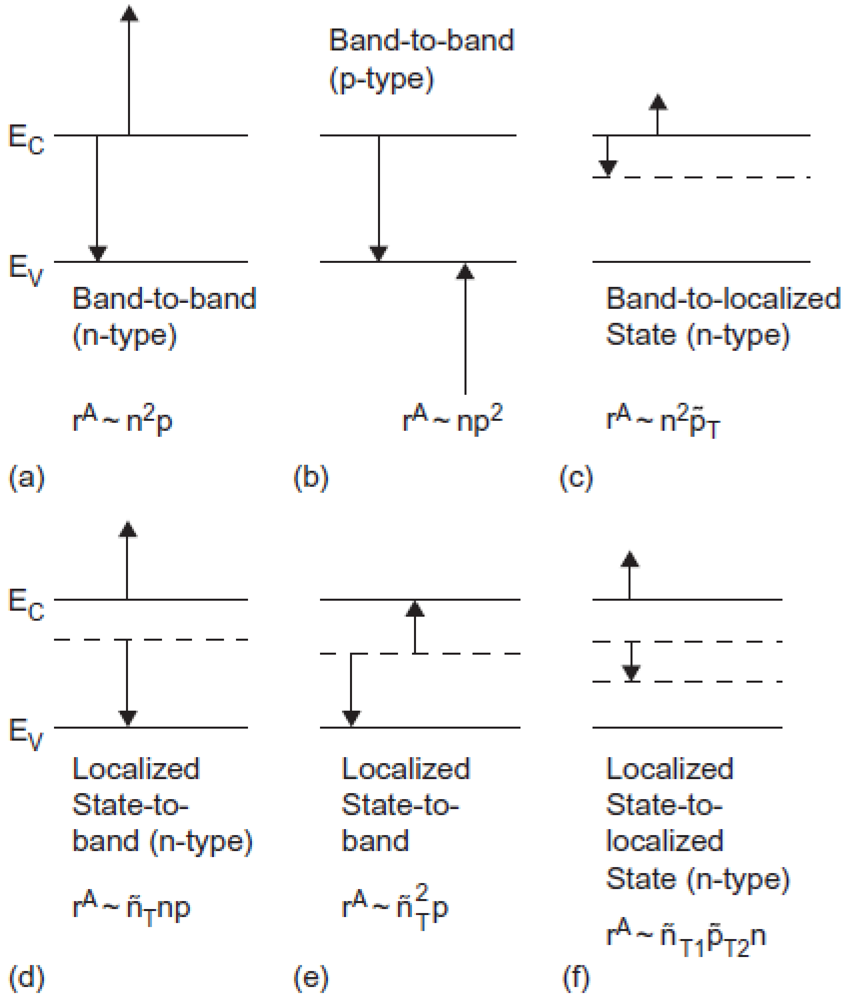

Figure 2.6: Some possible Auger transition processes in solids. [5]

2.1.3 Carrier Transport

In semiconductors electrons and holes are subject to the classical processes of drift and diffusion. Drift is a motion of charged carriers under the influence of an applied electric field. The drift current densities for holes and electrons can be expressed as:

$$J_p^{drif} = q\mu_p pE = -q\mu_p p\nabla\phi \qquad (2.\ 10)$$

$$J_n^{drif} = q\mu_n nE = -q\mu_n n\nabla\phi \qquad (2.\ 11)$$

Where μ_p and μ_n are hole and electron mobility separately[25].

Electrons and holes in semiconductors tend to diffuse from areas of high concentration to areas of low concentration. Diffusion current density is given by:

$$J_p^{diff} = -qD_p \nabla p \tag{2. 12}$$

$$J_n^{diff} = qD_n \nabla n \tag{2. 13}$$

D_p and D_n are hole and electron diffusion coefficient respectively. The total hole and electron currents are the sum of drift and diffusion currents:

$$J_p = J_p^{drif} + J_p^{diff} = -q\mu_p p \nabla \phi - qD_p \nabla p \tag{2. 14}$$

$$J_n = J_n^{drif} + J_n^{diff} = -q\mu_n n \nabla \phi + qD_n \nabla n \tag{2. 15}$$

The total current is:

$$J = J_n + J_p \tag{2. 16}$$ [25]

2.1.4 Theoretical Analyses of Solar Cell Operations

The operation of most semiconductor devices can be described using semiconductor device equations. Here a generalized form of these equations will be given by the Poisson's equation [25]:

$$\nabla \cdot \varepsilon E = q\left(p - n + N\right) \tag{2. 17}$$

N is the net charge due to dopants and other trapped charges.

The continuity equations of holes and electrons are[25]:

$$\nabla \cdot J_p = q\left(G - R_p - \frac{\partial p}{\partial t} \right) \tag{2. 18}$$

$$\nabla \cdot J_n = q\left(R_n - G + \frac{\partial n}{\partial t} \right) \tag{2. 19}$$

where G is the optical generation rate of electron–hole pairs. Current densities of electron and hole are[25]:

$$\vec{J}_p = -q\mu_p p \nabla\left(\phi - \phi_p\right) - kT\mu_p \nabla p \tag{2. 20}$$

$$\vec{J}_n = -q\mu_n n \nabla\left(\phi + \phi_n\right) + kT\mu_n \nabla n \tag{2. 21}$$

ϕ_p and ϕ_n are band parameters that account for a spatially changing electron affinity and band gap [28]. These two terms can usually be ignored in nondegenerate homostructure photovoltaic cells. [25]

Now we can write down a set of equations to describe all physics processes taking place in photovoltaic cells. This math system includes

1. Poisson's equation;
2. The continuity equations for electrons and holes.
3. Eqs. 2.20 and 2.21

By solving the complete set of coupled partial differential equations with proper boundary conditions, we can establish the cell's current density-voltage (J-V) characteristic which is important for cell performance evaluation and optimization. With the help of computer numerical solutions numerical solutions of these coupled nonlinear equations can be obtained.

However, with proper assumptions and simplification analytical solutions can be obtained. Assume in a uniformly doped semiconductor, the band gap and electric permittivity is constant. In the steady state, the semiconductor equations will reduce to:

$$\frac{d\vec{E}}{dx} = \frac{q}{\varepsilon}\left(p - n + N_D - N_A\right) \tag{2. 22}$$

$$q\mu_p \frac{d}{dx}\left(p\vec{E}\right) - qD_p \frac{d^2 p}{dx^2} = q\left(G - R\right) \tag{2. 23}$$

$$q\mu_n \frac{d}{dx}\left(n\vec{E}\right) + qD_n \frac{d^2 n}{dx^2} = q\left(R - G\right) \tag{2. 24}$$

Considering that in quasi-neutral regions the electric field is very small, under low-level injection ($\Delta p = \Delta n \ll N_A, N_D$), the drift current can be ignored with respect to the diffusion current. Therefore R in p-type region simplifies to

$$R = \frac{n_P - n_{P0}}{\tau_n} = \frac{\Delta n_P}{\tau_n} \tag{2. 25}$$

and in n-type region to

$$R = \frac{p_N - p_{N0}}{\tau_p} = \frac{\Delta p_N}{\tau_p} \tag{2. 26}$$

Δp_N and Δn_P are the excess minority-carrier concentrations. τ_n and τ_p are minority-carrier lifetimes. Equations 2.22 and 2.23 thus reduce to

$$D_p \frac{d^2 \Delta p_N}{dx^2} - \frac{\Delta p_N}{\tau_p} = -G \tag{2. 27}$$

$$D_n \frac{d^2 \Delta n_P}{dx^2} - \frac{\Delta n_P}{\tau_n} = -G \tag{2. 28}$$

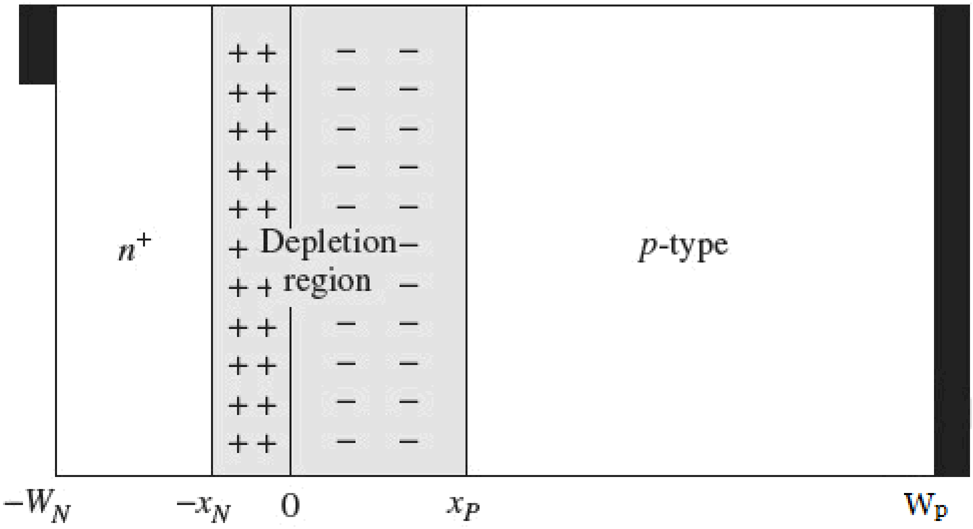

Figure 2.7: Simple photovoltaic cells structure used to analyze the operation of a photovoltaic cells. Free carriers have diffused across the junction ($x = 0$) leaving a space-charge or depletion region practically devoid of any free or mobile charges. The fixed charges in the depletion region are due to ionized donors on the *n*-side and ionized acceptors on the p-side.[25]

In a basic photovoltaic cells as established in figure, the structure is divided into four parts: n-type quasi-neutral region($-W_N<x<-x_N$);p-type quasi-neutral region($x_P<x<W_P$); depletion region($-x_p<x< W_P$). Taking surface recombination into consideration the boundary conditions are:

$$\frac{d\Delta p}{dx}=\frac{S_{F.eff}}{D_p}\Delta p(-W_N)\,,\ x=-W_N \qquad (2.\ 29)$$

$$\frac{d\Delta n}{dx} = -\frac{S_{BSF}}{D_n}\Delta n(-W_p)\,,\, x= W_P \qquad (2.\ 30)$$

$$p_N\left(-x_N\right) = \frac{n_i^2}{N_D}e^{qV/kT} \quad ,x= -x_N \qquad (2.\ 31)$$

$$n_P\left(x_P\right) = \frac{n_i^2}{N_A}e^{qV/kT} \quad ,x= x_P \qquad (2.\ 32)$$

2.1.5 Photovoltaic cells operation and performance parameters

Based on previous works of planar PVCs and algebraic manipulation, general expressions can be written:

$$I = I_{sc} - I_{01}(e^{qv/kt} - 1) - I_{02}(e^{qv/2kt} - 1) \qquad (2.\ 33)$$

Isc is the short-circuit current. I_{01} is the dark saturation current due to recombination in quasi-neutral region; I_{02} is the dark saturation current due to recombination current in space-charge region. The detailed expression of I_{01} and I_{02} will not be listed, considering they can be found in many text books and not quite relevant to the discussion below. For a good Si PVC, I_{02} can usually be ignored. The current-voltage (I-V) characteristic of typical PVC is plotted in figure 2.8.

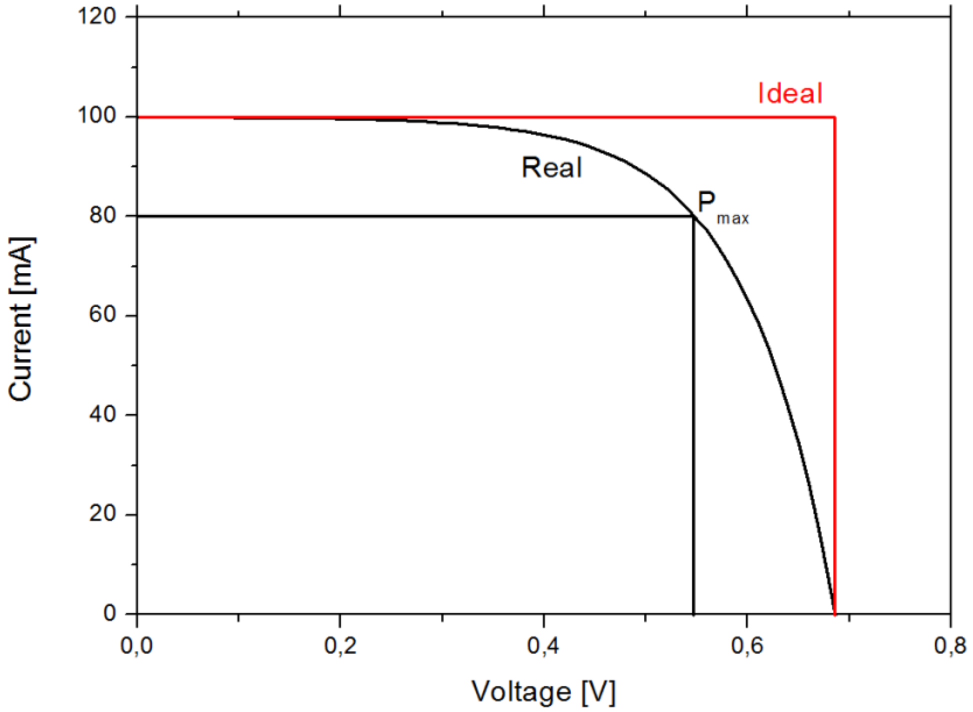

Figure 2.8: The ideal and real I-V curves [24]

At open circuit, the I=0, open circuit voltage (Voc) can be written as:

$$Voc = \frac{kT}{q}\ln\frac{I_{sc}+I_{01}}{I_{01}} \tag{2. 34}$$

As the measure of the "squareness" of the I-V curve, fill factor, is defined as:

$$FF = \frac{P_{MP}}{I_{sc}V_{oc}} = \frac{I_{MP}V_{MP}}{I_{sc}V_{oc}} \tag{2. 35}$$

I_{MP} and V_{MP} are the current and voltage at maximum power point respectively. The PVC power conversion efficiency η is defined as:

$$\eta = \frac{P_{MP}}{P_{IN}} = \frac{FFV_{oc}I_{sc}}{P_{IN}}\ \eta = \frac{P_{MP}}{P_{IN}} = \frac{FFV_{oc}I_{sc}}{P_{IN}} \tag{2. 36}$$

where P_{IN} is the incident power of light.

Parasitic resistance effects

The equivalent circuit model of a photovoltaic cell is shown in figure2.9.

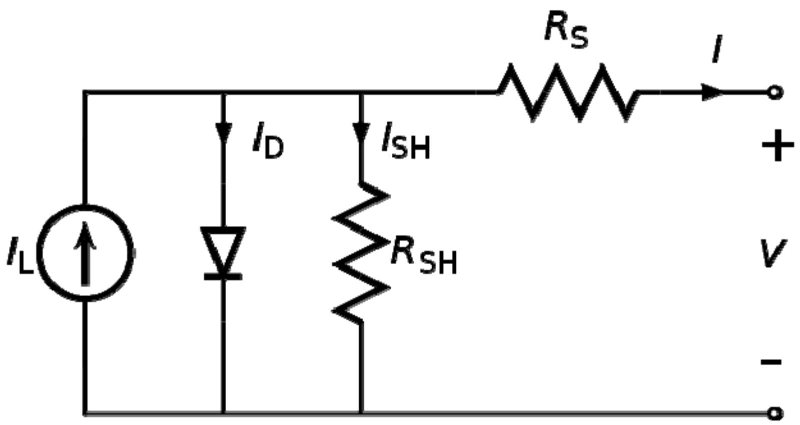

Figure 2.9: Equivalent circuit of a solar cell[25].

1. *Rs* represents the series resistance. It comes from the bulk resistance of the material and the metal-semiconductor interface and can be expressed as:

$$Rs = \frac{1}{\frac{dI}{dV}}\Big|_{V=V_{oc}} \tag{2. 37}$$

The influence of *Rs* on I-V curve is the reduction of *Isc* and *FF*, as shown in figure 2.10.

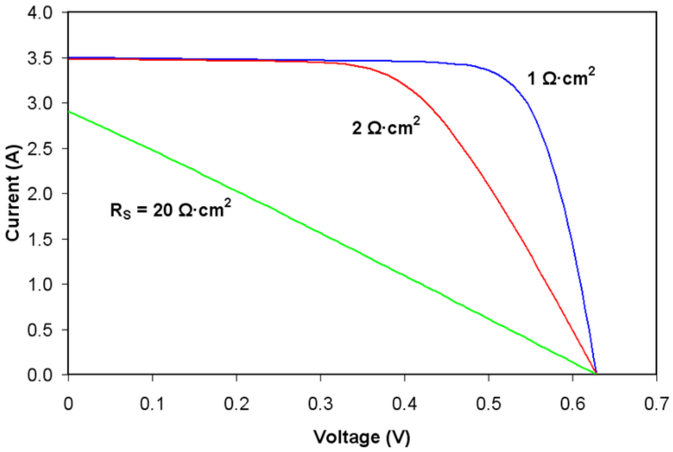

Figure 2.10: Solar cell I-V curve as a function of specific series resistance[29].

2. *Rsh* represents the shunt resistance, which comes from the leakage current across

the junction which can be expressed as:

$$Rsh = \frac{1}{\frac{dI}{dV}}|_{V=0} \quad (2.\ 38)$$

The influence of *Rsh* is reduction of *Voc* and *FF*, as shown in figure 2.11

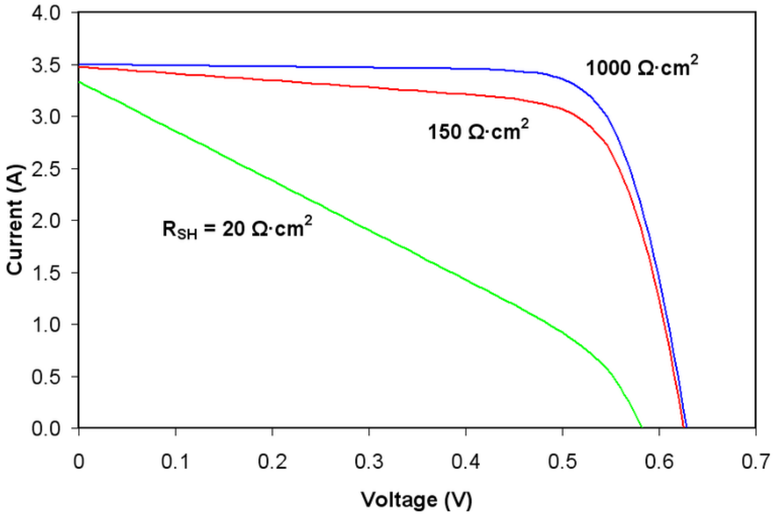

Figure 2.11: Solar cell I-V curve as a function of specific shunt resistance[29, 30].

2.1.6 Trade off between diffusion distance and absorption length.

In conventional planar photovoltaic cells, as shown in figure 2-1, light penetration depth is characterized by 1/α, where α is the absorption coefficient of material. The mean free path of generated minority carries is given by the diffusion length, L_n. In the case in figure 2.12, light penetrate deep into cell, but the carrier diffusion length is too short, therefore collection of all photo-generated carriers is impossible[12]. In order to solve the contradicting requirements between the diffusion distance and absorption length, the configuration of a radial p-n junction solar cell is proposed, which will be discussed in the following sections.

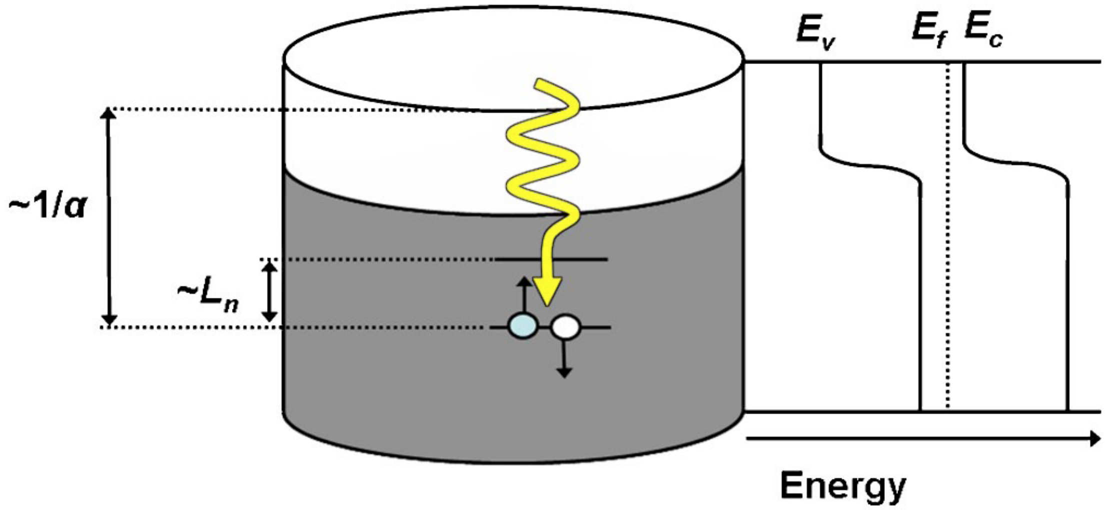

Figure2.12: Conventional planar photovoltaic cell is a *p-n* junction device. Light penetration depth is characterized by,1/α, where α is the absorption coefficient; while the mean-free path of generated minority carriers is given by diffusion length L_n [12].

2.2 Theory of radial p-n junction PVC

Radial p-n junction basing on nanowires offer long absorption length while maintaining short path for charge collection (as shown in figure 2.13). In the conventional planar geometry, charge collection will be restricted by minority carrier diffusion length if materials with limited absorption efficiency are used as the absorption layer. This means that increasing the absorption layer thickness does not result in the corresponding improvement in cell efficiency, since the generated charges recombine before being collected. Radial p-n junctions may be able to solve this problem. In this geometry, incident light can be absorbed vertically and generate charges that are collected horizontally, therefore the absorption and carrier collection efficiency are simultaneously guaranteed[12]. The scheme of radial p-n junction solar cell is shown in figure 2.14.

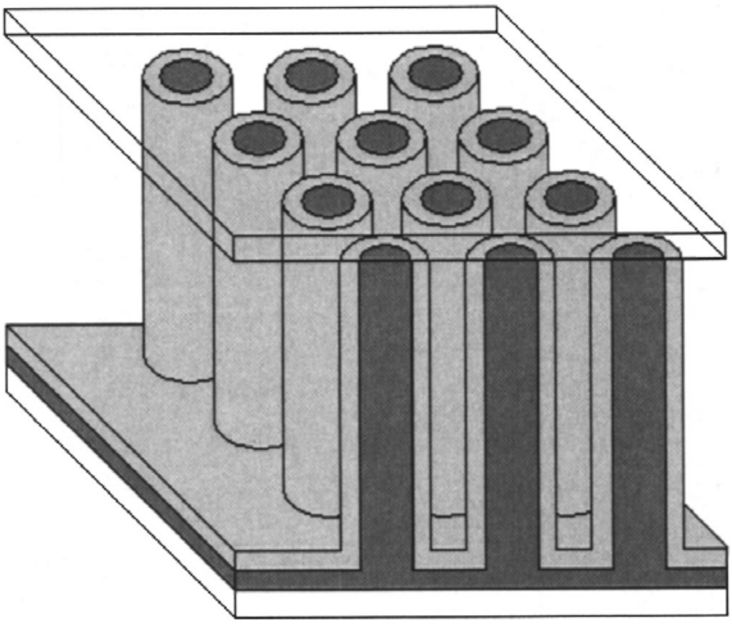

Figure 2.14: Schematic cross-section of the radial p-n junction nanorod cell. Light is incident on the top surface. The light grey area is n type, the dark grey area p type[12].

The theory of radial p-n junction PVC is based on Kayes's comparison of the device physics principles of planar and radial p-n junction nanorod solar cells. The schematic cross-section of a radial p-n junction PVC, as well as the corresponded generalized band diagram, is illustrated in figure2.15. Silicon p-n junction will be discussed here. Assumption of the cell structures and calculations are listed below:

1. P-N junction is abrupt;
2. Depletion approximation valid;
3. Light incident normally;
4. Shockley-Reed-Hall recombination is the only recombination mechanism;
5. Surface recombination is taken into consideration;
6. Purely radial carrier transport is assumed in the radial p-n junction.

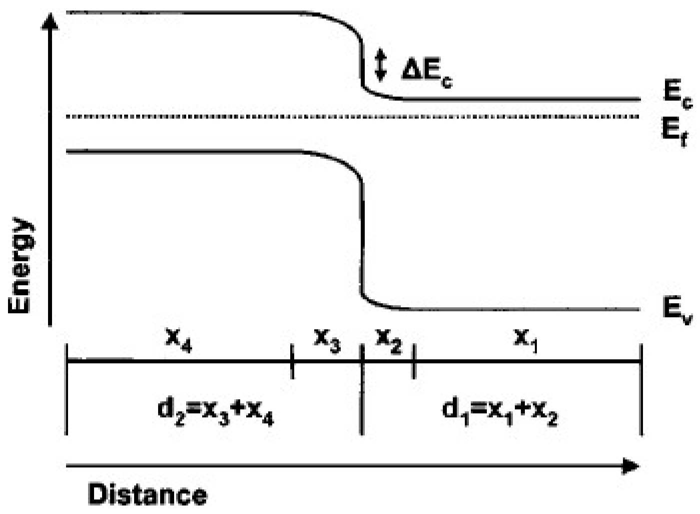

Figure 2.15: Generalized band structure for a heterojunction nanorod structure. Shown are the conduction and valence band energies, E_c and E_v, as well as the Fermi energy E_f. ΔE_c is the discontinuity in the conduction band energy, which may be nonzero for a heterojunction. The example cells in this paper are homojunctions, and so $\Delta E_c = 0$. The x axis shows the schematic division of the cell into four regions: the quasi-neutral part of the n-type material (of width x_1), the depleted part of the n-type material (of width x_2), the depleted part of the p-type material (of width x_3), and the quasi-neutral part of the p-type material (of width x_4)[12].

Quasi-neutral p-type region

The minority carrier diffusion equation (eq. 2.27) can be applied:

$$\nabla^2 \triangle n - \frac{\triangle n}{L_n^2} = \frac{\partial^2 \triangle n}{\partial r^2} + \frac{1}{r}\frac{\partial \triangle n}{\partial r} - \frac{\triangle n}{L_n^2} = -\frac{\alpha_2 \Gamma_0}{D_n} e^{\alpha_2 x} \tag{2. 39}$$

α_2 is the absorption coefficient of p-type material, Γ_0 is the incident photon flux. The boundary conditions are:

$$\triangle n(0) = finite \tag{2. 40}$$

$$\triangle n(x_4) = n_0 (e^{qv/kT} - 1) \tag{2. 41}$$

The current density in p-type quasi-neutral region:

$$J_p(z) = -qD_n \frac{\partial \triangle n}{\partial r}|_{r=x_4} \tag{2. 42}$$

Quasi-neutral n-type region

In this region the minority carrier equation is:

$$\nabla^2 \triangle p - \frac{\triangle p}{L_p^2} = \frac{\partial^2 \triangle p}{\partial r^2} + \frac{1}{r}\frac{\partial \triangle p}{\partial r} - \frac{\triangle p}{L_p^2} = -\frac{\alpha_2 \Gamma_0}{D_p} e^{\alpha_2 x} \tag{2. 43}$$

α_1 is the absorption coefficient of p-type material. The boundary conditions are:

$$\triangle p(R - x_1) = P_0 \left(e^{qv/kT\vartheta} - 1 \right) \tag{2. 44}$$

$$S_p \triangle p(R) = p_0 \frac{\partial \triangle p}{\partial r}|_{r=R-x_1} \tag{2. 45}$$

The current density in p-type quasineutral region:

$$J_n = \frac{2(R - x_1)\int_0^L J_n(z)\,dz}{R^2} \tag{2. 46}$$

$$J_n(z) = qD_p \frac{\partial \triangle p}{\partial r}\Big|_{r=R-x_i} \qquad (2.47)$$

Depletion region

$$J_{dep.p.ph} = q\Gamma_0(1-e^{\alpha L})\frac{d_2^2 - x_4^2}{R^2} \qquad (2.48)$$

$$J_{dep.n.ph} = q\Gamma_0(1-e^{\alpha L})\frac{(d_2 + x_2)^2 - d_2^2}{R^2} \qquad (2.49)$$

With parameters of the assumed photovoltaic cells structure, simulation can be performed by computer. Since this thesis mainly focus on the fabrication and characterization of radial p-n junction photovoltaic cells, instead of simulation, the detailed simulation results will not be discussed here. However, several general trends from Kayes and Atwater's theoretical analyses turn out to be useful guiding principles for the photovoltaic cells design and fabrication. They are listed below[12]:

Table2.1 General Conclusion of the Influence of Rod Length and Rod Radius on Radial p-n Junction PVCs Performances

	Rod Length(L) Increase		Rod Radius(R) Increase	
Jsc	$L<\frac{1}{\alpha}$	$L>\frac{1}{\alpha}$	*R<Ln*	*R>Ln*
	Increase	Plateau	Change Slowly	Decrease Sharply
Voc	Decrease		Increase	

In spite of the fore-mentioned advantages in light absorption and carrier collection, photovoltaic cells with vertically aligned silicon nanowires are less sensitive to impurities than planar ones [12]. In addition to the advantages in carrier collection, silicon nanowire arrays also demonstrate significant reduction of light reflection over the full spectrum above the band gap, as shown in figure 2.16. This unique antireflection property helps to enhance the light absorption in photovoltaic cells[31].

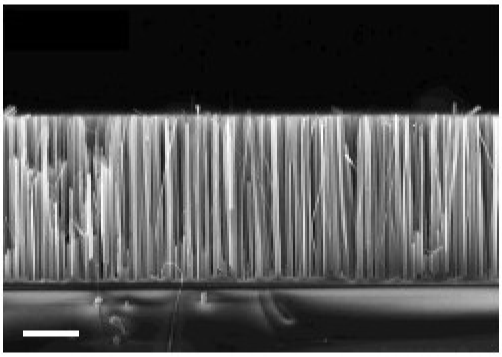

(a)

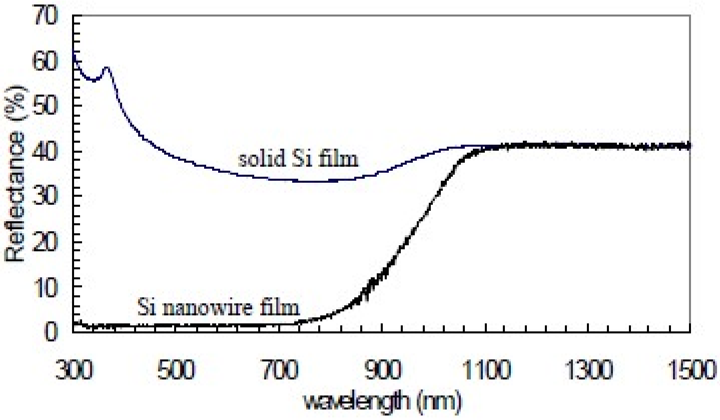

(b)

Figure 2.16: (a)Cross-sectional SEM image of an ~10 micron thick nanowire array on a glass substrate with The length of the micron marker is 4 microns. (b) Reflectance data for sample in (a) before and after wet etched[31].

2.3 Silicon nanostructure fabrication

Generally, approaches to synthesize silicon nanowires (SiNWs) for silicon nanowire-based PVCs can be placed into two categories. One is vapor phase growth, usually with catalysts [7, 11]. Another approach is selective etching process, also known as top-down method, which is more advantageous to synthesize verticalsilicon nanowires in relatively large scale. The top-down approaches rely on various selective etching and nanoimprint techniques and are versatile in fabricating different nanostructure arrays.

2.3.1 Nanospheres Lithography

Among different top-down approaches, nanospheres lithography is widely used to fabricate ordered silicon nanowires arrays. The key steps are shown in Figure 2.17. Various techniques can be used to fabricate monolayer masks, including controlled evaporation of solvent[32, 33], spin-coating[34], self-assembly on the water surface[35], Langmuir-Blodgett assembly[36], and so on. Self-assembly on the water surface and Langmuir-Blodgett assembly seems to be suitable and can be easily controlled for the fabrication of large scale ordered monolayer synthesis.

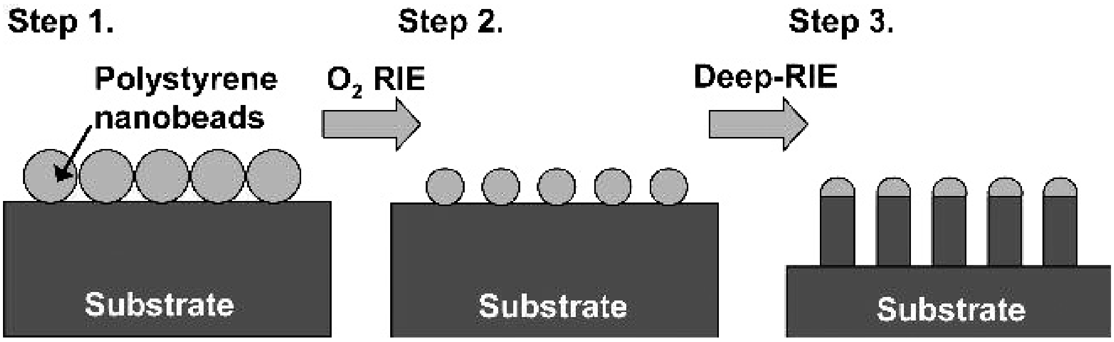

Figure 2.17: Schematic diagram of nanopillar fabrication by nanosphere lithography. Step 1: spin coat a hexagonally close packed monolayer of polystyrene beads on substrates. Step 2: tailor the size of the beads' 'resist' by oxygen plasma etching. Step 3: etch the exposed semiconductor areas by deep reactive ion etching using the 'Bosch' process.[37]

Reactive Ion Etching (RIE) plays an important role in the NSL process, since it is used for both the reduction of polystyrene diameter as well as deep etching of silicon. Other selective silicon etching techniques have also been developed, among them metal-induced silicon etching has attracted considerable attention and has been widely used in nanostructure fabrication[38].

2.3.2 Metal Catalyzed Electroless Etching

Metal catalyzed electroless etching (MCEE) is a versatile solution-based silicon etching method. As shown in figure 2.18, with patterned noble metal film on top of the silicon wafer surface, silicon contacting with metal will be etched away, therefore various silicon nanostructure can be created. According to Peng, K.Q. the metal enhanced silicon etching is an electrochemical reaction, the reactions are shown below[39, 40]:

At noble metal:

$H_2O_2 + 2H^+ = 2H_2O + 2h^+$

$2H^+ + 2e^- = H_2\uparrow$

At silicon:

$Si + 4h^+ + 4HF = SiF_4 + 4H^+$

$SiF_4 + 2HF = H_2SiF_6$

Overall reaction:

$Si + H_2O_2 + 6HF = 2H_2O + H_2SiF_6 + H_2\uparrow$

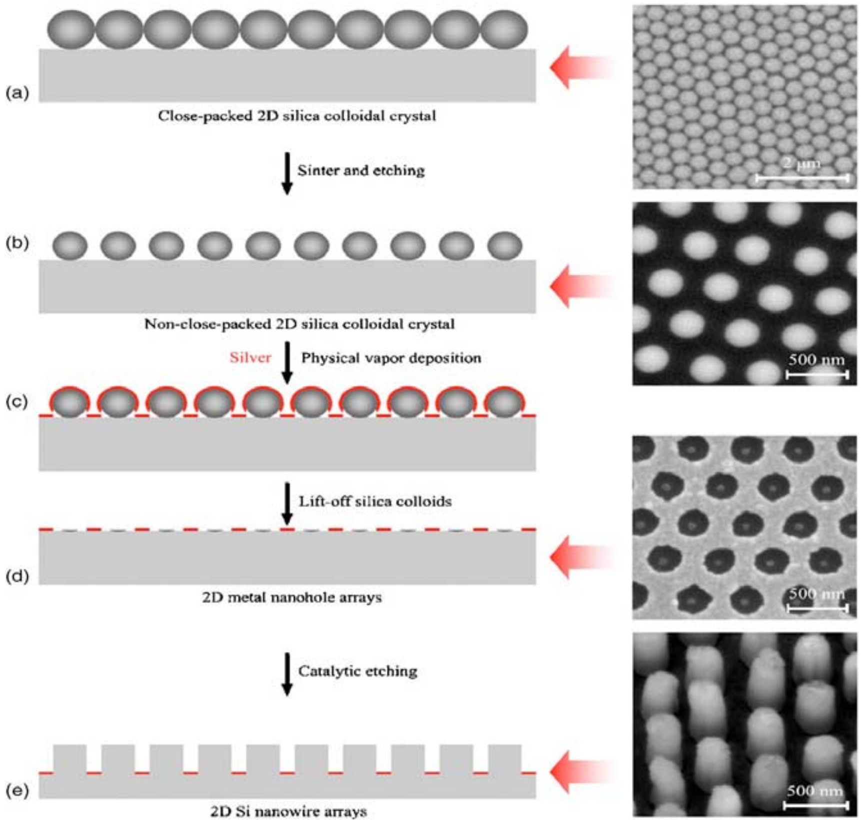

Figure 2.18: Schematic illustration of the experimental procedures for fabricating large-area arrays of ordered SiNWs: (a)deposition of monolayer silica colloidal crystal template on silicon surface; (b) fabrication of 2D non-close-packed silica colloidal crystals on silicon surface; (c) deposition of silver layer on silicon surface through the non-close-packed colloidal crystal template; (d) formation of regular silver nanohole arrays by removing silica colloids by brief ultrasonication in water; and (e) formation of SiNWs by catalytic etching. The corresponding SEM micrographs on the right show the monolayer silica colloidal crystal template (a) ,the 2D non close-packed silica colloidal crystal template(b), the silver film with periodic nanohole arrays (d), and ordered SiNW arrays produced using catalytic silver film with periodic nanoholes (e).[41]

Noble metal can be used to catalyze silicon etching including: Ag, Pt, Au and Cu, among which Au and Pt are expensive metal therefore not preferred in the photovoltaic cell fabrication. Though copper is cheap, it dissolves in the etching solvent due to the existence of H_2O_2, therefore is not preferred in the above mention process to create the desired silicon pattern. However, while applying voltage Cu can catalyze silicon etching (without H_2O_2). This electrochemical etching method will be discussed in the following chapters.

As an aqueous solution based technique, MCEE serves as a versatile tool to fabricate large scale silicon nanostructure with simple equipment, and at low cost. Metal-enhanced silicon etching can be used as a silicon etching technique in nanospheres lithography (NSL), thereby creating ordered silicon nanowires arrays, as illustrated in figure 2.18 [41].

2.4 Characterization technique

2.4.1 Nanostructure Surface morphology characterization

Images of silicon nanostructure are vital to the control and optimization of nanostructure dimensions and morphology. In our experiments, we systematically characterized the morphology of the nanostructure as a function of the etching parameters. Scanning Electron Microscopy (SEM) is the most frequently used technique[42].

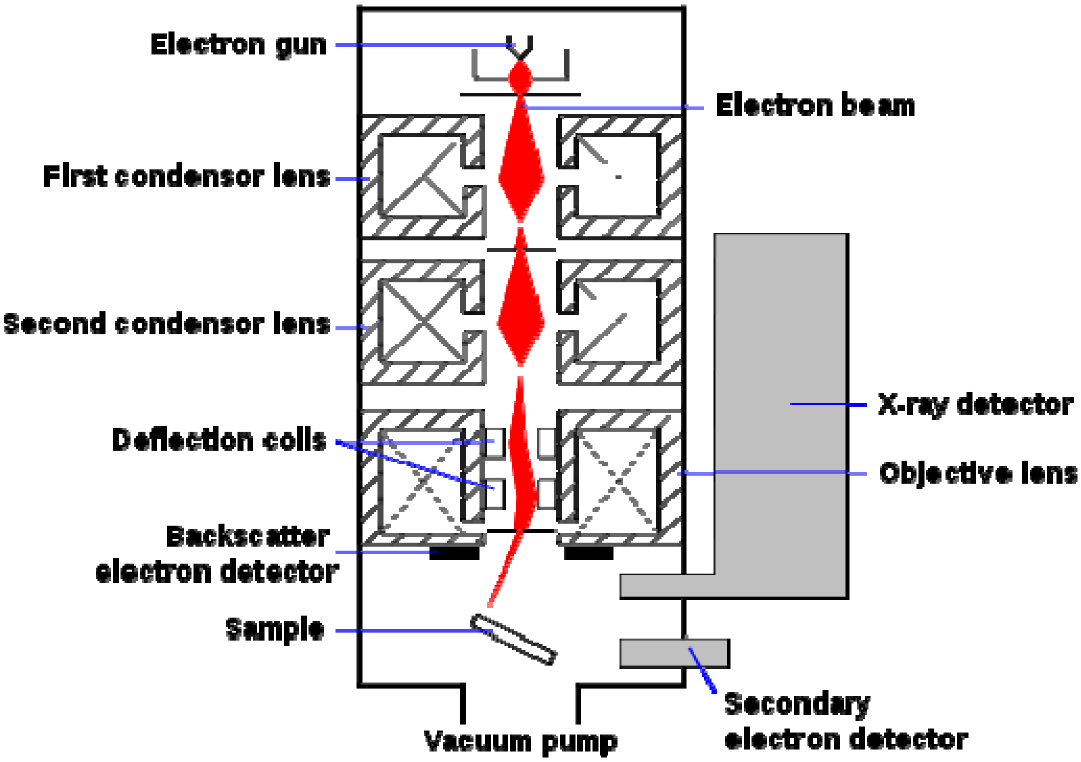

Figure 2.19: Diagram of SEM[42]

SEM is a fast and convenient method to obtain surface images. The basic scheme of SEM is shown in figure 2.19. In a vacuum chamber, while condensed electron beam scans the sample surface (the sample should be conductive), the emitted secondary electrons are collected by a detector and images are generated. In this project, samples with silicon nanostructures which are conductive can be directly placed in an SEM chamber and scanned to obtain images[42].

2.4.2 SIMS

Time-of-Flight Secondary Ion Mass Spectrometry (ToF-SIMS) is a surface-sensitive analytical technique. By using pulsed ion beam to remove molecules from the surface of the sample, the removed molecules (secondary ions) are then accelerated into a "flight tube" and their mass is determined by measuring the time at which they reach the detector. The diagram of ToF-SIMS is shown in figure 2.20[43].

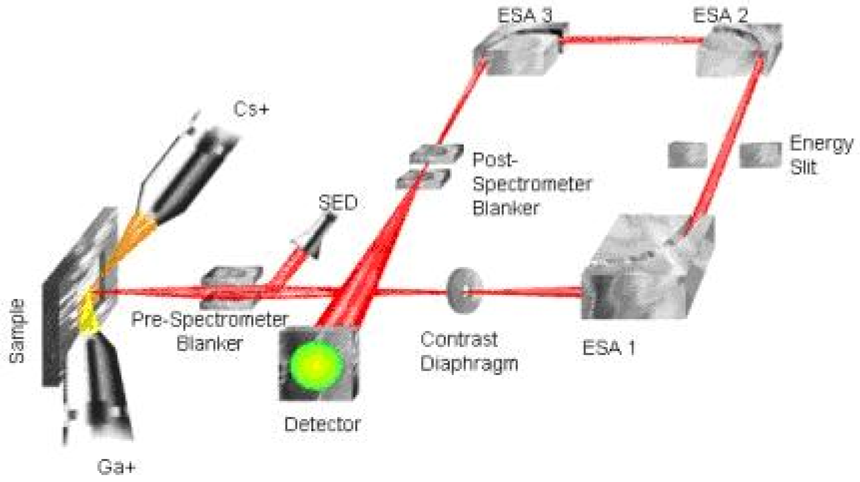

Figure 2.20: The diagram of ToF-SIMS[43]

ToF-SIMS is widely used in material analysis and characterization, and the three main application modes are:

1. Elemental/Molecular Surveys;
2. Elemental/Molecular Maps; and
3. Depth Profiles.

With high sensitivity, it can be used to detect trace elements or compounds on the order of ppm to ppb for most species. As to depth profiling, it has a resolution of the order of tens of nanometers[43].

3 Experiment

In this chapter the experimental setup and methods to fabricate random nanohole radial junction PVCs are described. The characterization methods are also discussed, as well as the development of Cu catalyzed electrochemistry etching is illustrated.

3.1 Ag film thermal annealing to form nanosized islands

Silver film annealing and MCEE processes are combined to generate silicon nanohole structures. E-beam is used to deposit Ag films on Si wafer. The thermal treatments are performed in rapid thermal annealing (RTA). SEM is used to obtain images of Ag islands. Since the profile and location of silicon nanoholes are decided by the Ag islands which form after thermal Ag film thermal annealing, the understanding of the influence of the fabrication conditions on the sizes and inter-islands distances of the Ag islands is necessary to have a better control of the structure. Therefore, the morphology of thermal annealing formed Ag islands is investigated as functions of Ag film thickness, annealing time, annealing temperature, and silicon wafer surface properties.

3.1.1 The influence of silicon wafer treating

To fabrication the silicon nanohole structures the Si wafers were first ultrasonically cleaned in acetone and isopropanol for 5 mins. The silicon wafers were then treated in a 1:1:5 solution of NH_4OH : H_2O_2 : H_2O at 75°C for 15 mins followed by DI water rinse. This produces a hydrophilic surface for the Si wafer[44]. Another silicon wafer with hydrophobic surface, serving as the control, was prepared by etching the surface using dilute HF. Thin Ag films (5nm) were deposited on the as-prepared silicon wafers by e-beam, followed by RTA at 800°C for 10mins in N_2 ambient for the formation of Ag nanoislands.

3.1.2 The influence of Ag film thickness

To investigate the influences of Ag film thickness on the size and inter-distance of Ag islands, 3nm, 5nm, 10 nm and 15nm, films were deposited separately on hydrophilic Si wafer (treatment steps are illustrated in section 3.1.1). Then the samples were annealed at 800°C for 10mins in N_2 ambient and the SEM images of each sample were then obtained.

3.1.3 The influence of annealing time & temperature

To investigate the influences of annealing temperature on the size and inter-distance of Ag islands, 5nm Ag films were deposited on Si wafers. Then thermal annealing were carried out at 400°C, 500°C, 600°C, 700°C, and 800°C for 10 min separately. Also 8nm Ag was deposited on Si wafer and annealed at 500°C for 60s and 600s to investigate the influence of annealing time on the morphology of the Ag nano-clusters.

3.1.4 Exploration of the Ag island size limitation

Previous experiments showed thicker Ag film resulted in larger Ag islands sizes. In order to determine the larges size of Ag island can be formed by Ag film thermal annealing, 30nm, 70nm, 150nm, and 300nm Ag film were deposited on hydrophilic silicon wafer, then annealed at 800°C. The annealing time was prolonged to 30mins for the 30nm sample and 1h for other samples to guarantee sufficient reaction time.

3.2 Silicon nanohole etching and PVC substrate preparation

3.2.1 Metal catalyzed electroless etching

The nanoholes were fabricated following Peng's procedure[45, 46]. The p-type silicon wafer (8-12Ωcm), covered with nanometer scale silver islands, was immersed in a mixture of 10ml 4.8 M HF and 0.4 ml 35% H_2O_2 for 5 mins. The Ag islands will serve as local electrodes to facilitate the MCEE process in which the silicon under Ag coverage will be etched.

3.2.2 Ag particle surface passivation

It is noted that the presence of large number of small holes can be found on the Si surface after the MCEE process, as shown in Figure 3.1 (a), which do not match the profile of the Ag islands. This is attributed to partial dissolution of the Ag islands into smaller granules during the etching process [47] as illustrated in Figure 3.1 (b). Our experiment showed that heating up the samples in air at 100°C for ~10 mins prior to the MCEE process can lead to significant reduction of the roughening of surface and significant improvement in the morphology of the nanostructure as clearly shown in Figure 3.2(a) and a typical cross section of the nanoholes is shown in Figure 3.2 (b). Such improvements may be attributed to the formation of a dense oxide film on the surface of the Ag islands, due to the heating step in air[48], which can mitigate the dissolution of Ag islands in the etching process.

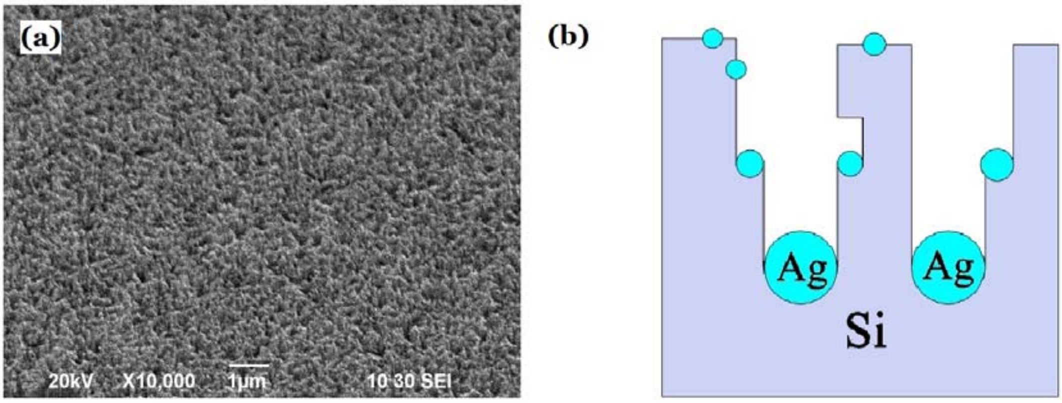

Figure 3.1: (a) The morphology of a typical sample directly etched in HF and H_2O_2 mixture after RTA[49]; (b) Ag dissolved and re-crystallized in the etching process forming silver grains on the side walls

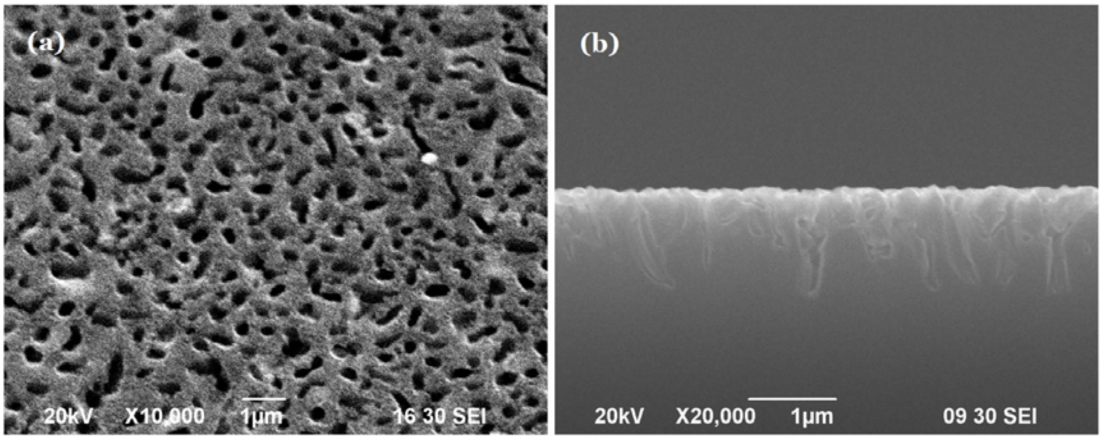

Figure 3.2: (a) Typical sample etched after forming an oxide film on the Ag surface, the nanoholes show good resemblance to the pattern of the Ag nano-islands[49]; (d) Cross-section of a typical nanohole structure.

3.2.3 Electrochemical etching of Ag and Cu

Considering Cu is a more cost-effective material compared to silver, it will be a significant improvement if it can be used in the nanohole etching for PVC fabrication. In the MCEE, Cu can serve as a local electrode to catalyze silicon etching, however it will be oxidized by H_2O_2 soon after contact with etching solution. Therefore we tried to use Cu to catalyze Si electrochemistry etching in HF without using H_2O_2.

Similar to the Ag-assisted MCEE process, Cu pattern should first be formed on Si wafers. According to our preliminary experiment results, thermal annealing of Cu film was unable to generate Cu islands on Si wafer, therefore Cu circular patterns were fabricated utilizing photo lithography and lift off technique. Photo resist was first spin coated on cleaned Si wafers, and then photolithography was performed to form holes on the photo resist. The exposure time is 300s and the development time 15s. E-beam was used to deposit 40nm Cu on the samples, followed by lift-off in acetone and cleaning in isopropanol followed by DI water rinse. Diameter of Cu the plate is 2um, and the inter plate distance is 4um.

Electrochemical etching of Cu was performed following the procedure described by Huang *et al*[50]. The back surface of the Si wafer was in contact with an Al foil, and the front surface is in contact with the etching solution (3.4% HF) in the electrochemistry cell. A Platinum wire was used as the counter electrode. 0.4 V bias was applied to the cell for 15mins, 30 mins and 60 mins. As described by Huang *et al.*, who first reported Cu assisted Si etching in 2010, detailed etching voltage were not mentioned [50], therefore 1V and 5 V voltage was also applied. The etched wafers were examined under SEM.

Si wafer with thermal annealing formed Ag islands on top was also loaded in the same electrochemistry cell, serving as a control sample. 0.4V bias was applied for 15mins. After raisin in the DI water to get rid of HF on the surface, SEM images of these samples were also taken.

3.3 PVC fabrication & Characterization

Based on the Si random nanohole structures, radial p-n junctions are formed via gas phase diffusion and PVCs were formed by fabricating front and back contact. Systematic investigations of the influence of nanostructure dimension and doping conditions on solar cell performance were conducted. In this section the PVC fabrication and characterizations will be discussed in detail.

3.3.1 Substrate preparation for PVC fabrication

Based on previous experimental results, we can adjust Ag islands size and inter-distance by variation of different parameters. In this project we conducted detailed investigations on the influences of the nanohole dimensions and doping conditions on the cell performances.

The fabrication conditions are listed in the Table 3.1 below. For the first batch of PVC (111) wafers were used, and in the second batch (100) Si wafers were used, for further improvement and optimization.

Table 3.1: Fabrication Condition of PVC basing on p-type Si(111) wafer

No.	Ag Thickness/ nm	Annealing Time/min	Carrier Gas Flow Rate /sccm	Diffusion Time/s
T3-250	3	10	250	600
T3-500	3	10	500	600
T5-250	5	10	250	600
T5-500	5	10	500	600
T5-750	5	10	750	600
T5-1000-2	5	10	1000	600
T10-250	10	10	250	600
T10-500	10	10	500	600
T10-750	10	10	750	600
T10-1000	10	10	1000	600
T15-250	15	10	250	600
T15-1000	15	10	1000	600

Table 3.2: Fabrication Condition of PVC basing on p-type Si(100) wafer

No.	Ag Thickness/ nm	Annealing Time/min	Carrier Gas Flow Rate/sccm	Diffusion Time/s
P0T30-600	30	15	1000	600
P0T30-800	30	15	1000	800
P0T30-1000	30	15	1000	1000
P0T30-1200	30	15	1000	1200
P0T70-600	70	30	1000	600
P0T70-800	70	30	1000	800
P0T70-1000	70	30	1000	1000
P0T70-1200	70	30	1000	1200
P0T150-600	150	60	1000	600
P0T150-800	150	60	1000	800
P0T150-1200	150	60	1000	1200

3.3.2 Gas phase diffusion to form p-n junction

Gas phase diffusion, which is widely used in the fabrication of high efficiency cells were adopted as Si doping method using $POCl_3$ source. Such doping method was chosen to guarantee conformal doping of the nanostructures on p-type silicon wafer.

The diagram of diffusion equipment is shown in figure 3.3. High purity N_2 as the carrier gas was passed into a liquid $POCl_3$ source which is used as an n-type dopant. At high temperature (>600°C) $POCl_3$ decompose into PCl_5 and P_2O_5, the PCl_5 will be further oxidize into P_2O_5 by adding O_2. P_2O_5 further reacts with silicon, as given below:

$$2P_2O_5 + 5Si = 5SiO_2 + 4P\downarrow$$

On the surface of the nanostructures phosphor silicate glass therefore forms, from which P diffuse into silicon and form n-regions on the surface of the nanostructures.

Prior to loading samples into the diffusion furnace, pre-diffusion cleaning was performed by immersing the substrates in buffered HF for 1min and subsequently cleaned with DI water. After drying in N_2 flow, the substrates are loaded into the diffusion furnace. The doping process was carried out at 865°C for 600s at N_2 flow rates of 50sccm, 500sccm, 750sccm, and 1000sccm in the first batch of PVC; at 865°C for 600s, 800s, 1000s, 1200s with N_2 flow rates of 1000sccm for the second batch. The diffusion conditions are also listed in table 3.1 and 3.2 in section 3.2.4.

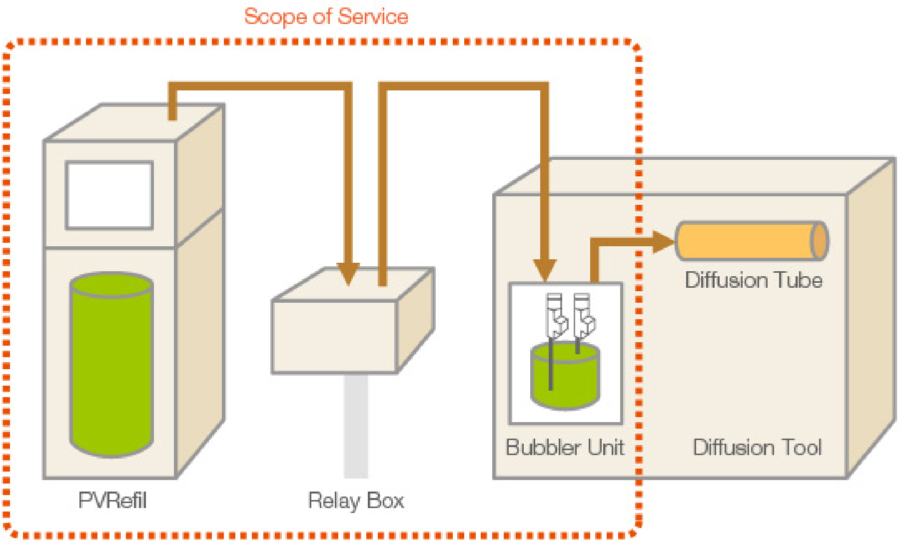

Figure 3.3: Diagram of gas phase diffusion equipment

3.3.3 Front & Back contact

In order to fabricate front contact, the phosphor silicate glass was removed in dilute HF, followed by the sputtered deposition of 200nm thick ITO and Al/Au metal grid. To remove the rear parasitic p-n junction, 10 microns of silicon on the backside was polished away. Aluminum was then deposited on the backside to form the back contact. To prevent the aluminum layer from oxidation, 10nm Au was deposited on top of the Al. Good ohmic contact was formed by annealing the cells at 350°C for 1h. The PVC structure is shown in figure3.4. A typical PVC is shown in figure 3.5

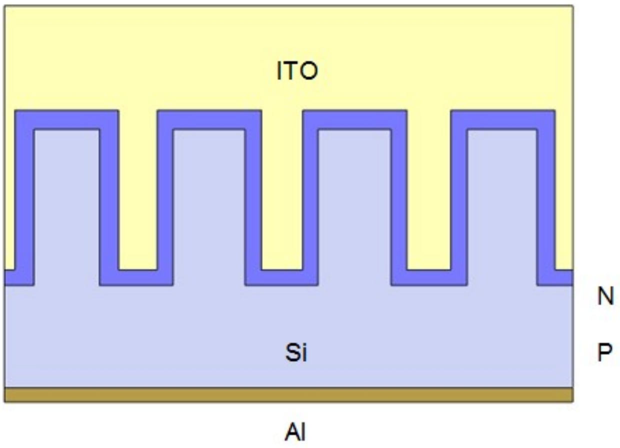

Figure 3.4: Scheme of solar cell structure.

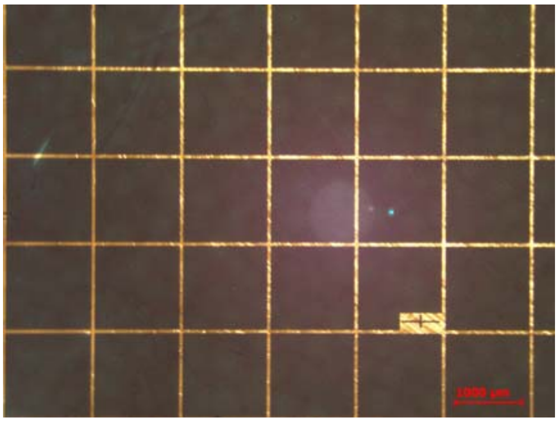

Figure 3.5: Photo of a typical solar cell with metal grid on the front surface.

3.3.4 Cell performance measurement

I-V curve contains significant information of the performance of PVCs, therefore the I-V curve of each device was measured under 1.5AM solar simulator. The PVCs were placed on Al foil to form good back contact. A gold wire was used to probe the metal grid on the front side. *Voc, Isc, FF* and efficiency were calculated and recorded.

3.3.5 Reflectance measurement

The incorporation of nanostructure will effectively reduce the reflectance, or increase light absorption of solar cells[18]. The measurement of reflectance can indicate the light trapping property of nanohole structures of different dimensions. The reflectance spectra of silicon substrate with nanostructure fabricated from different conditions were measured from 1100nm to 300 nm using Hitachi U-4100 Spectrophotometer. Polished silicon wafer was served as control sample.

4 Results and Discussion

In this part the experimental results of Ag film annealing, MCEE etching, and PVC characterization are shown in three parts correspond to the arrangement in chapter 3, and discussions are made following the demonstration of experimental results.

4.1 Ag film thermal annealing to form nanosized islands

Self-assembled Ag nano-islands can be formed by Rapid Thermal Annealing (RTA) of thin Ag films deposited on the Si surface. Silver thickness, annealing temperature, annealing time are all adjusted systematically to obtain different morphology and the influence of these parameters are discussed below.

4.2 The influence of Si wafer property

Following experiment steps in section 3.1.1, the SEM image of annealed Ag film on hydrophilic and hydrophobic Si wafers are shown in figure 4.1. The existence of exceedingly small Ag islands on hydrophobic Si wafer subsequent to the RTA process can be found in Figure 4.1(a). On the other hand, on Si samples treated in a NH_4OH : H_2O_2 : H_2O=1:1:5 solution result in the formation of a thin SiO_2 layer on the surface of the Si wafer[44] with significantly larger Ag islands being formed. The result shows that Ag islands grown on hydrophilic Si surfaces are much larger in size and can be varied systematically by using different Ag film thickness as discussed in the following section[51, 52]. Therefore, using hydrophilic surface for the preparation of Ag nanoclusters is crucial for our purpose.

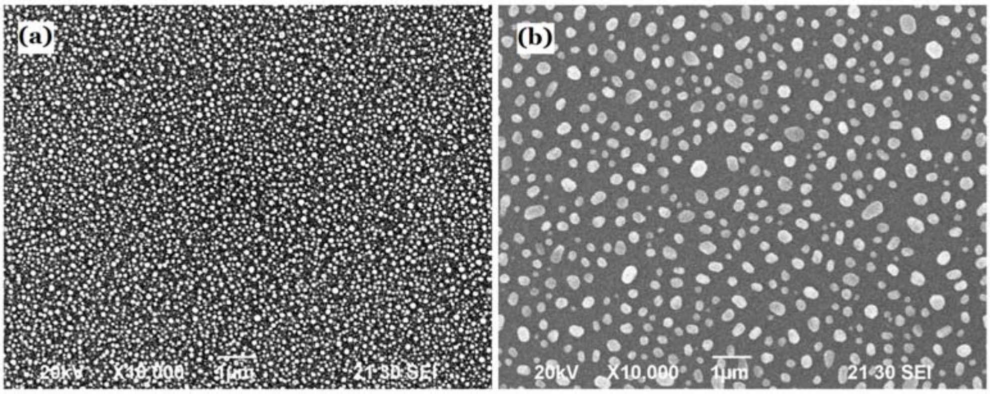

Figure 4.1: SEM images of (a) Ag nanoislands formed on RCA processed hydrophilic Si substrate; (b) the condition of Ag islands deposited on HF etched silicon substrate[49].

4.2.1 The influence of Ag film thickness

The SEM images of annealed Ag film of different thickness are shown in figure 4.2. The data demonstrates that the sizes and inter-distance of Ag islands increase with the thickness of the Ag film for Ag films deposited on hydrophilic Si wafer

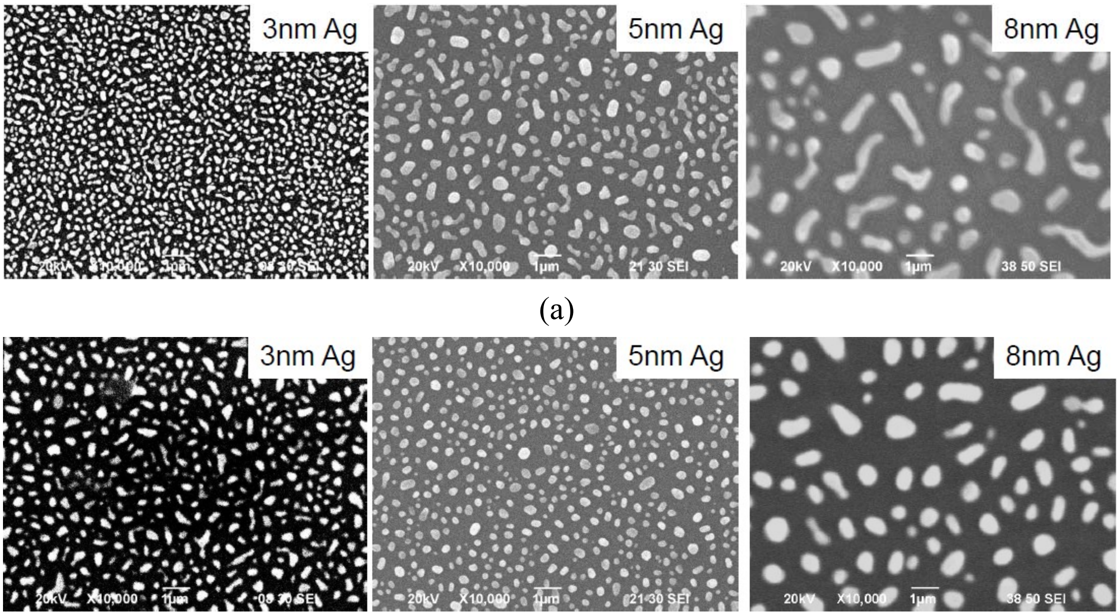

(a)

(b)

Figure 4.2: The influence of silver thickness
(a)500℃; (b) 800℃[49]. 10min

4.2.2 The influence of annealing time

The SEM images of Ag film for different annealing times are shown in figure 4.3.For a short annealing time, only holes were observed on the film, when the annealing time is prolonged to 600s, separate Ag islands can be observed subsequent to the annealing process. The data clearly demonstrate that sufficient annealing time is necessary for the Ag islands formation.

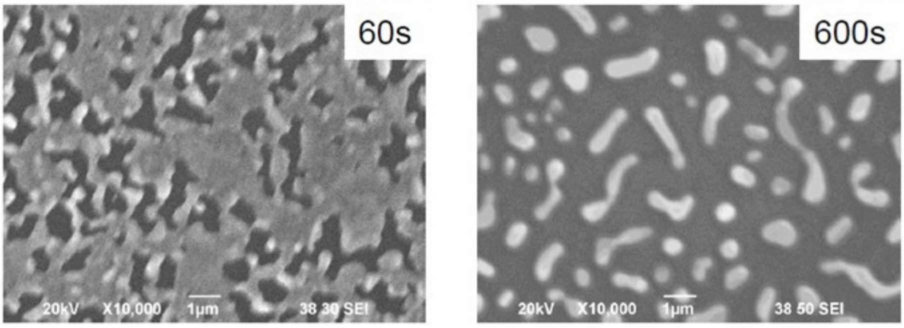

Figure 4.3: The influence of annealing time 8nm Ag, RTA 500℃, hydrophilic substrate[49].

4.2.3 The influence of annealing temperature

Figure 4.4 shows SEM images of 5 nm Ag film annealed at different temperatures for 10 mins. The effect of annealing temperature is not quite as obvious as the change of the Ag film thickness, yet higher temperatures tend to yield Ag islands with more rounded shape and more uniform sizes as shown in figure 4.4 below.

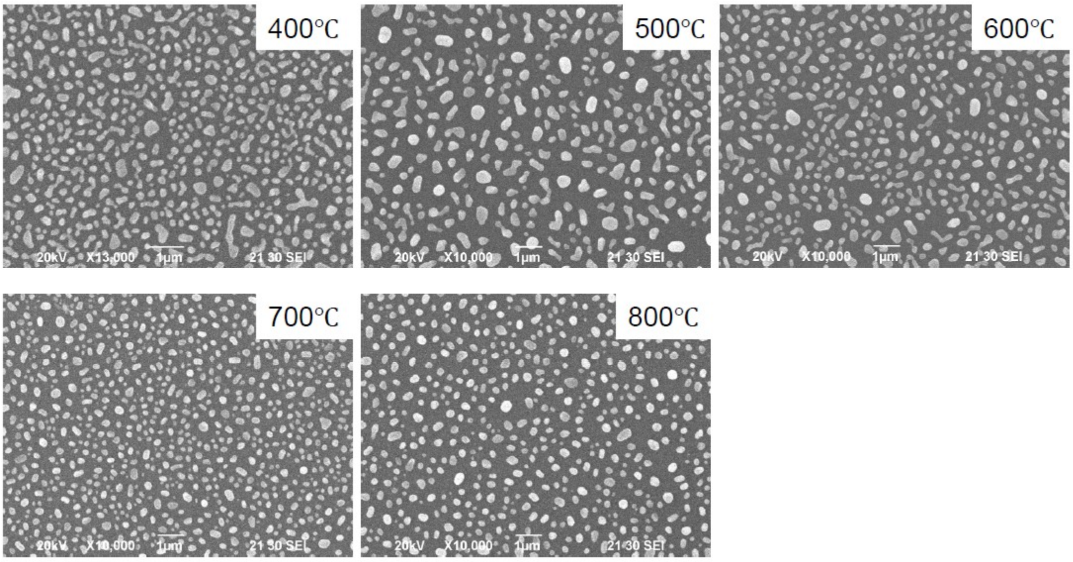

Figure 4.4: The influence of annealing temperature
5nm Ag, RTA 10min, hydrophilic substrate[49].

4.2.4 Maximum Ag film thickness of forming Nano-islands

As mentioned in the above section, the island size increases with Ag film thickness, however the sizes of these Ag islands can not increase indefinitely. Figure 4.5 and 4.6 show SEM images of Ag islands obtained by thermal annealing of 30nm and 70nm thick Ag films at 800℃ for 15 mins and 30mins separately. From these images we observe that as the Ag films become thicker, the average size of the islands increases correspondingly. However, the SEM images of 150nm thick Ag films annealed at 800℃ for 60mins, indicate failure in the formation of separated Ag islands in substantial portion of the sample even though the annealing time had been extended to 60mins. In areas where Ag islands were formed, the average size of Ag island is around 3-5μm. Further increase in the Ag film thickness, for example to 250nm in our experiment, no islands or holes can be formed even after 60mins of RTA at 800℃ as shown in figure 4.8. This indicates that the largest island size can be created by thermal annealing of Ag films is no more than several microns.

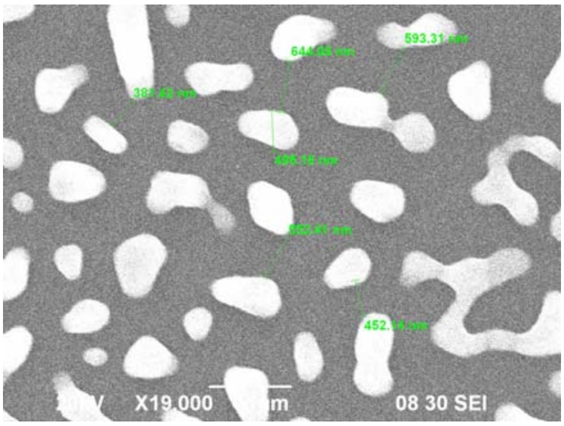

Figure 4.5: SEM image of 30nm Ag annealed at 800℃ for 30mins

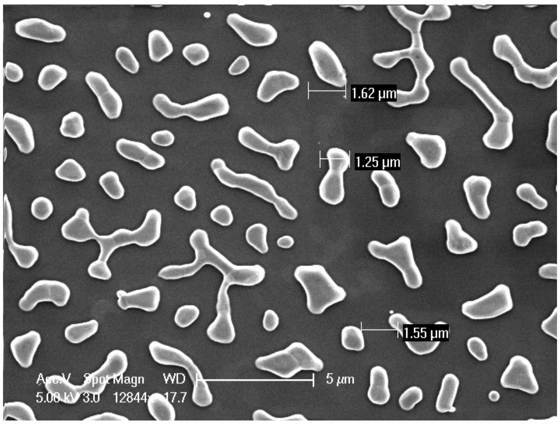

Figure 4.6: SEM image of 70nm Ag annealed at 800℃ for 30mins

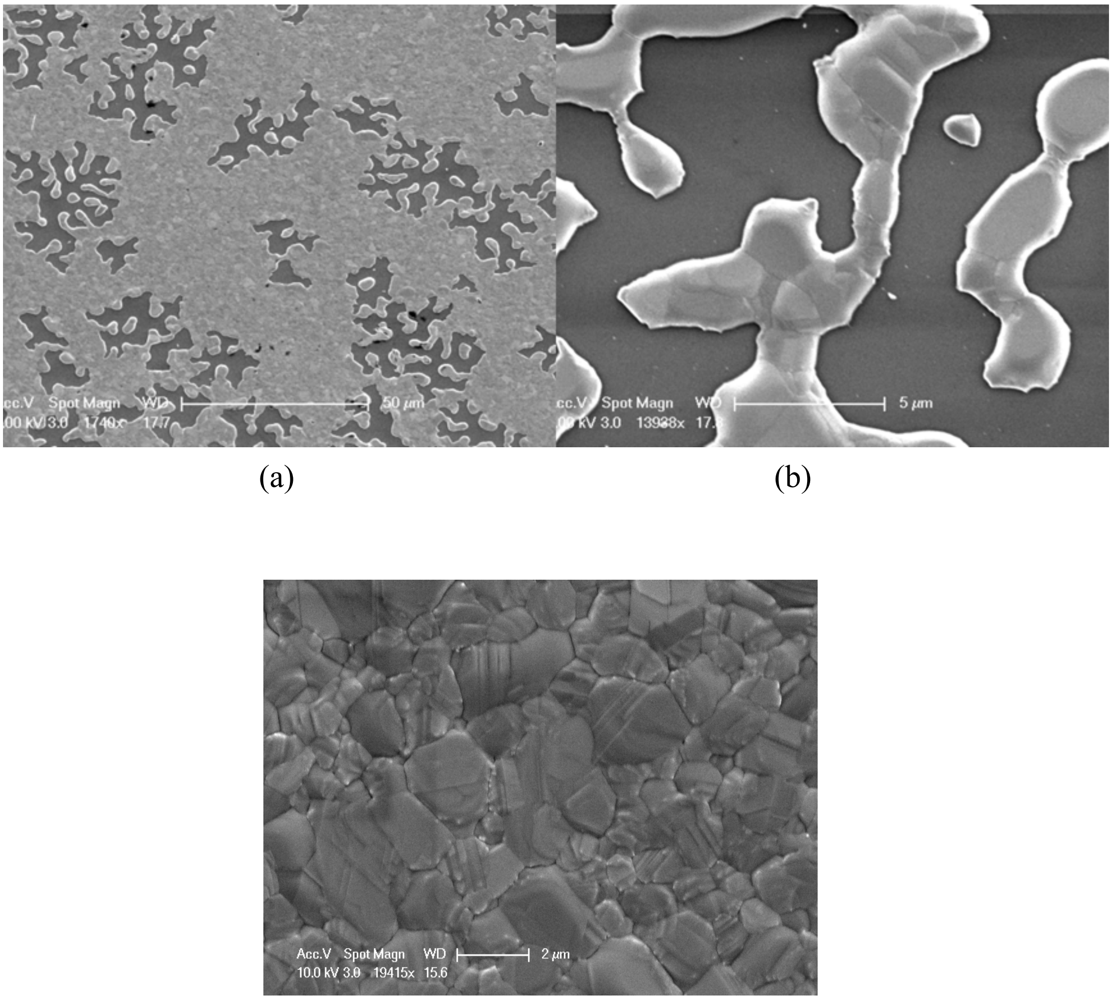

(a) (b)

(c)

Figure 4.7: SEM images of SEM images of: (a) and (b)150nm Ag annealed at 800℃ for 60mins; (c)SEM images of 300nm Ag annealed at 800℃ for 60mins

4.2.5 Summary of Ag nano-islands formation

The annealing process is illustrated in figure 4.8. During the RTA process holes were first formed on the Ag films which continue to expand and eventually resulted in the formation of nanometer-scale islands. From micro perspective, the Ag film can be viewed as the collection of small Ag granules. With trend to lower total surface energy, while the temperate rise up the Ag particles merge into larger particles from small ones to reduce total surface area, and finally form Ag islands, as illustrated in figure 4.8 (b). Sufficient annealing time is necessary to ensure the completion of this process. For thicker films the island formation process needs longer time which can be accelerated by conducting the process at higher temperatures.

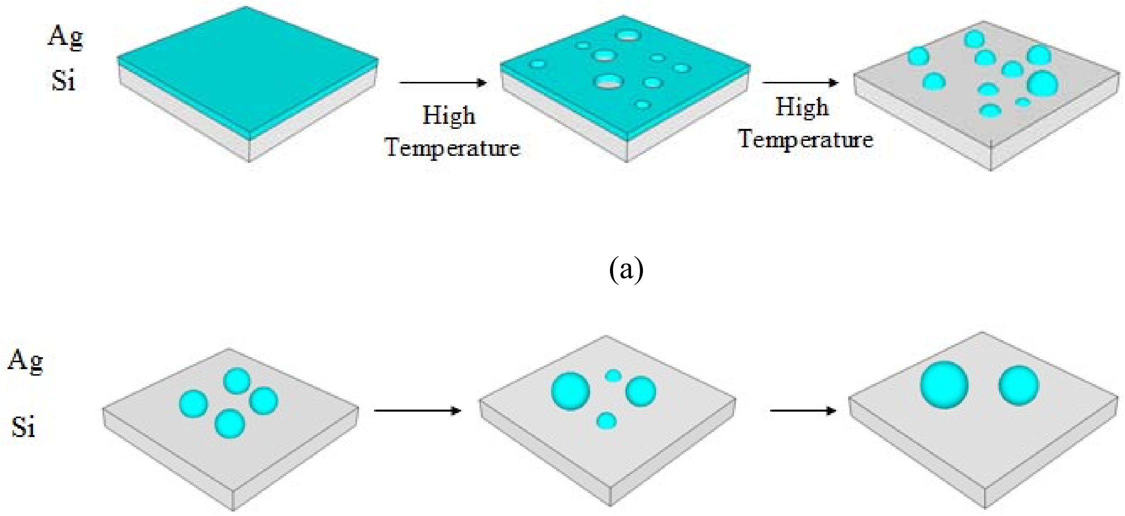

(a)

(b)

Figure 4.8: (a) Illustration of Ag film annealing process; (b) The small Ag particles assemble into larger ones.

Based on previous investigations on the effects of different fabrication parameters on the sizes and morphology of the Ag islands several conclusions can be derived as guidance for the adjustment of Ag island dimensions:

1. Hydrophilic Si wafer surface is crucial for the formation of separate Ag islands;
2. The sizes of the Ag islands increase with Ag film thickness;
3. Higher temperatures result in more uniform islands shape and size;
4. If Ag film is too thick nano-islands can not be formed.

4.3 Silicon nanohole etching

4.3.1 Metal catalyzed electroless etching

Ag islands formed in the RTA process will serve as local electrodes in the MCEE step, in which silicon is etched electrochemically and thereby creating nanoholes in the Si wafer. In figures 4.9 to 4.11 the SEM images of Si hole structures created from MCEE process using Ag islands of different sizes and silicon wafers with different orientations are shown. It is observed that generally speaking nanoholes etched from (100) (figure 4.11) wafers are more vertically oriented compared to those from (111) (figures 4.9 and 4.10) wafers. This is mainly due to the anisotropy of the MCEE process. According to investigations performed by Peng *et al.*[41] the etching direction tends to be vertical to the (100) surface. Therefore the holes in the (100) wafers are more vertical.

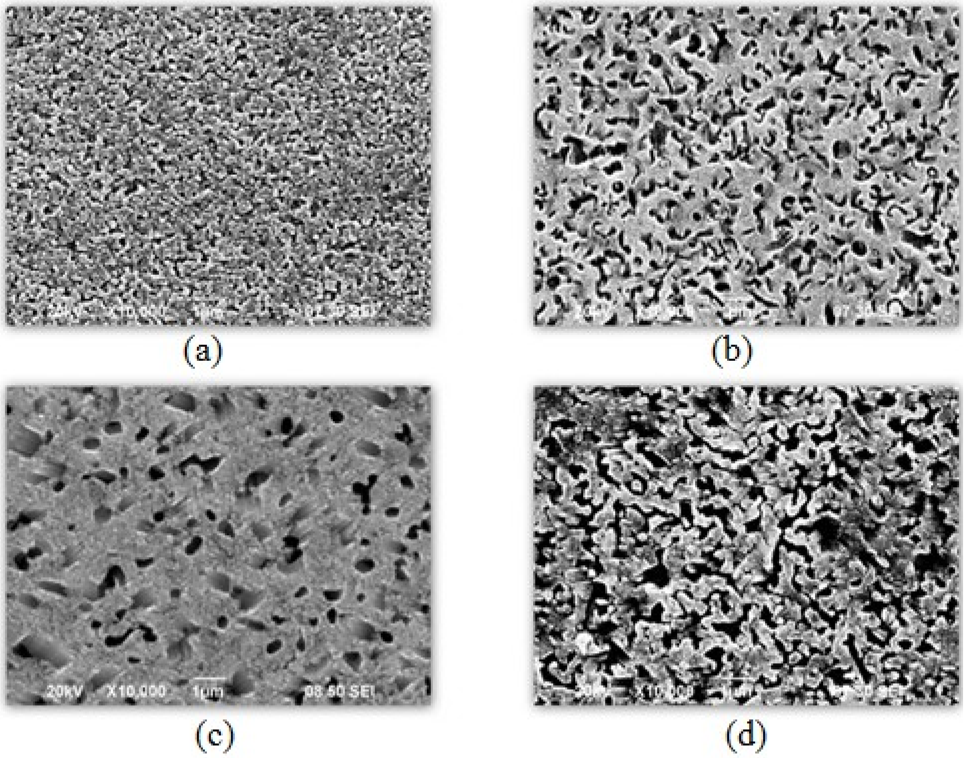

(a) (b)

(c) (d)

Figure 4.9: SEM images of top view of Si hole structure on p-type Si(111)wafer fabricated from Ag film of (a) 3nm; (b) 5nm; (c) 10nm; (d)15nm

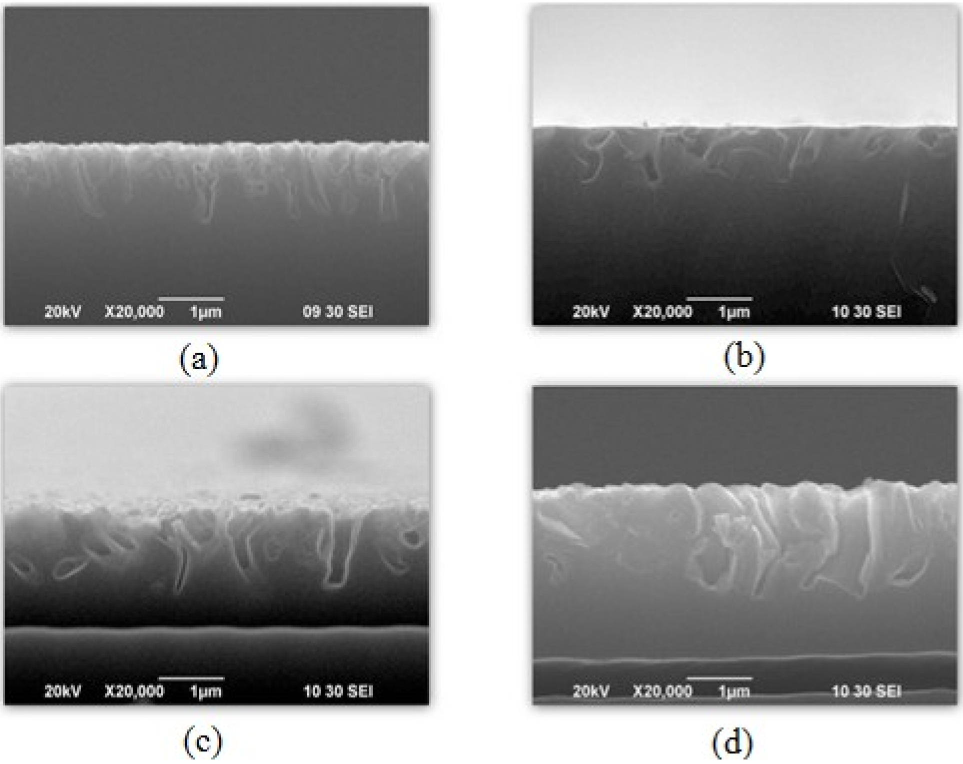

(a) (b)

(c) (d)

Figure 4.10: SEM images of cross-section of Si hole structure on p-type Si(111)wafer, fabricated from Ag film of (a) 3nm; (b) 5nm; (c) 10nm; (d)15nm

Theoretically, the profile of holes should correspond to the shape of the Ag islands, however, from the SEM images of the sample cross-section we observe that only the top part shows the similar shape with the Ag islands, and at the bottom of holes, both the shape and direction have been changed. This probably arises from the dissolution and recrystalization of Ag particles, this is illustrated in figure 3.1. Once the recrystalized Ag particles stick to the side wall of the holes, it will etch sideway and change the shape of holes.

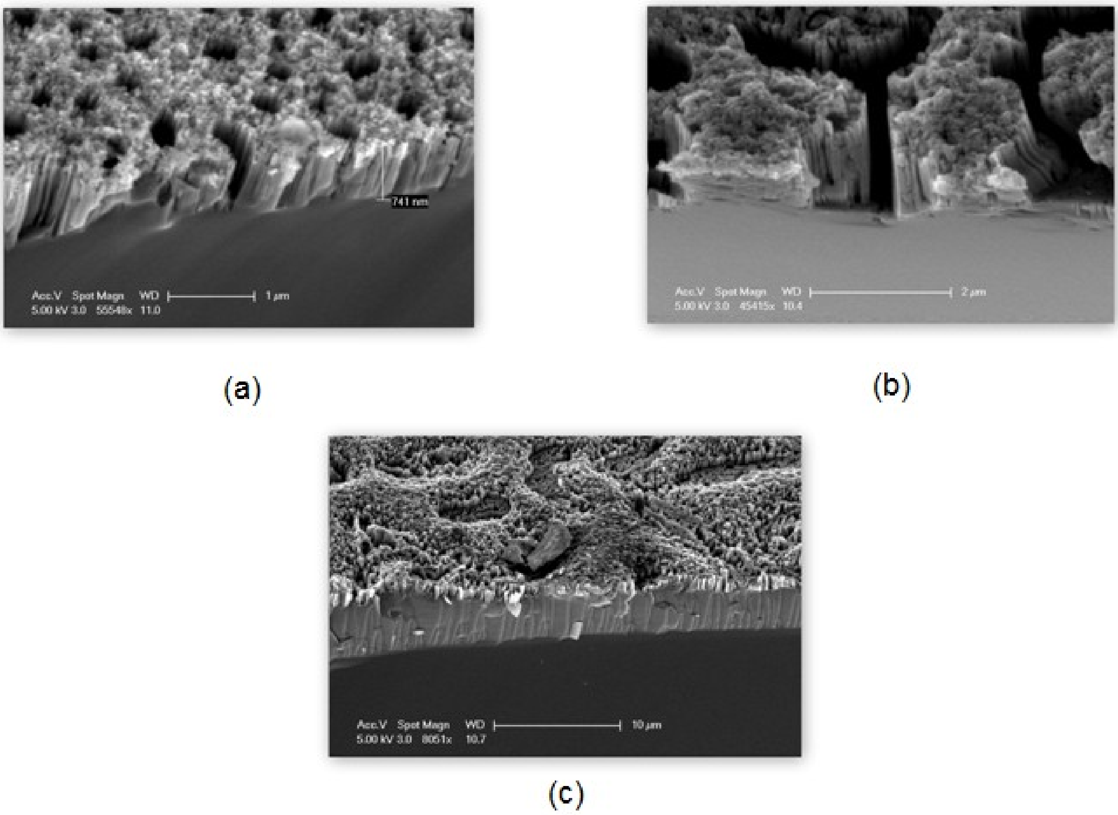

Figure 4.11: SEM images of cross-section of Si hole structure on p-type Si(100)wafer, fabricated from Ag film of (a) 30nm; (b) 70nm; (c) 150nm.

4.3.2 Electrochemical etching of Ag and Cu

In this section the experimental results on the electrochemical etching of Si using Ag and Cu as the metal catalysts will be introduced. In figure 4.12a we present the SEM images of Cu dots deposited on the surface of a Si wafer, in figure 4.12b we have illustrated the patterned Si surface subsequent to the electrochemical etching process under a 0.4 V bias. The SEM images of the wafers etched under 1V and 5V biases are also shown in figure 4.13 which demonstrate trenches between holes while using 0.4V bias, only the silicon directly under Cu coverage was being etched. It is believed that at high voltages silicon anodization takes place without the need for a metal catalyst, while at lower voltages a metal catalyst is needed for such a reaction. ,

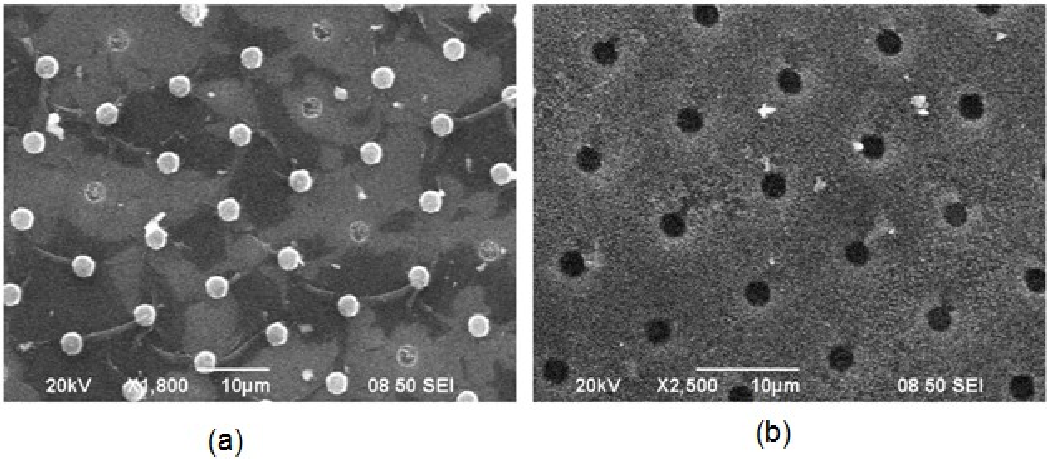

(a) (b)

Figure4.12: (a) SEM image of Cu pattern; (b) SEM image of Si surface after Cu catalyzed electrochemistry etching.

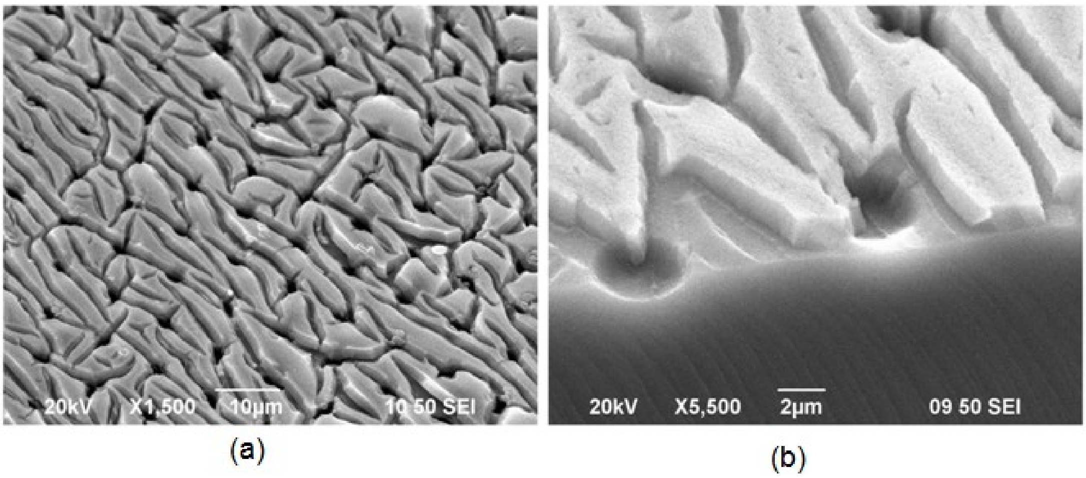

Figure 4.13: SEM image of trenches between nanoholes, 5V for 15 mins. .

Figure 4.14a and 4.14b show the cross-sections of the samples etched using Cu dots as the metal catalyst for etching times of 30 min and 60 min respectively. As the etching time increases there is no obvious corresponding increase in the depths of the silicon holes. The possibility of a reduction in the reaction rate due to the depletion of the electrolyte has been precluded as the current of the electrochemical cell had been kept constant for the entire period of the experiment.

From the cross sectional images of samples A and B we note that the hole depth for sample B is much less than expected. Although the etching time for sample B is double that of sample A the hole depth is only about 1.4 μm compared to 1.35 μm for sample A. It is suspected that simultaneous etching of the top surface and hole bottom is the cause for the observed phenomenon. Figure 4.15(a) illustrates a Si substrate with Cu pattern fabricated by nanospheres lithography and the SEM image taken after 30mins of Cu-induced electrochemical etching is shown in figure 4.15(b). After 30mins of etching, according to experimental results shown in figure 4.14, Si rods with >1µm height should be expected. However, from the experimental data, the average height of the Si rods is less than 200nm. Also, significant tapering is observed at the top of the rods. This also may be ascribed to the dissolution of Cu in the etching process. This phenomenon is also observed in the Ag MCEE process. Since Cu is more reactive than Ag, its dissolution is more significant than Ag. This may explain why the etching depth does not increase with etching time as observed in the experimental data presented in Figure 4.14.

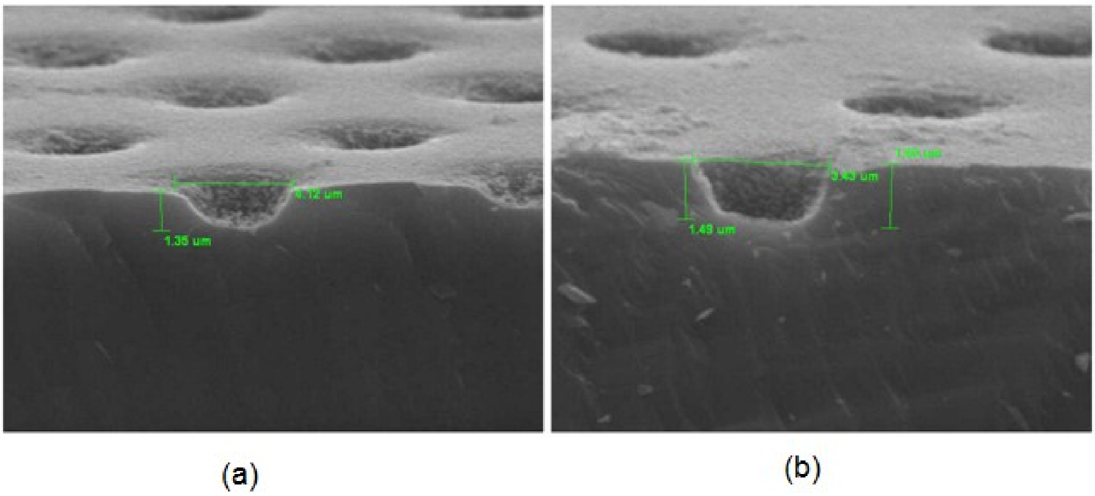

Figure 4.14: SEM image of Si wafer cross-section after Cu catalyzed electrochemical etching with 0.4V voltage for (a)30 mins; (b) 60 mins.

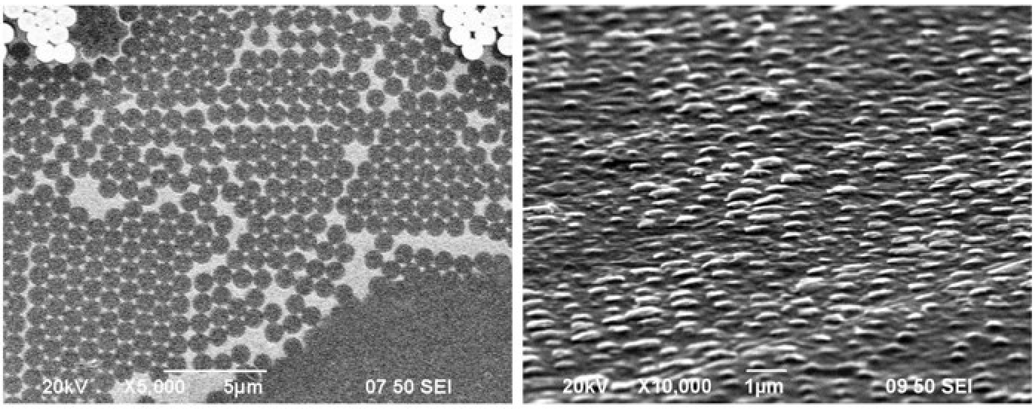

(a) (b)

Figure 4.15: SEM images of (a) Cu pattern on Si wafer fabricated by naospheres lithography; (b) After electrochemical etching at 0.4V for 30 min.

Figure 4.16 shows the Ag catalyzed electrochemical etching of silicon with about 2 µm holes at a bias voltage of 0.4V and an etching time of 60 min. The etching speed is much slower than the standard MCEE process in which no voltage is applied to the samples.

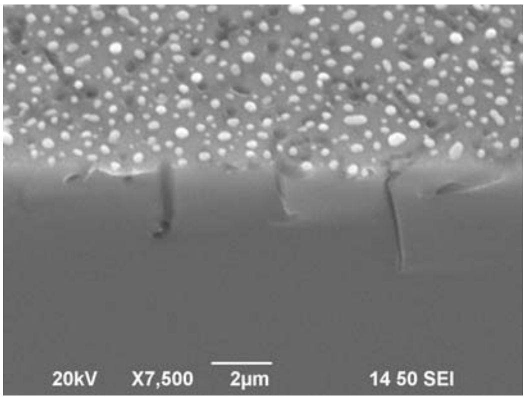

Figure 4.16: Ag catalyzed electrochemical Si etching, 0.4V for 60min

For the fabrication of radial p-n junctions , the silicon micro/nano structures with high aspect ratios are desired, therefore Cu electrochemical etching will not be the process of choice unless, optimization of the etching parameters (et. voltage, composition of etching solution) can be achieved to meet the stringent requirements of the devices.

4.4 PVC Characterization

We performed systematic investigations on the properties of the devices. Our experimental data show that the best device, was fabricated on a (100) p-type wafer, from which we obtained J_{sc} =11.84 mAcm^{-2}, V_{oc} = 490 mV, FF = 54.89% and η = 3.18%. The data demonstrate substantial improvements over other reported results on PVCs fabricated with random SiNW arrays[53-55]. The improvements in the device performance are attributed to the optimization of the nanohole dimension and the inter-hole distance, as well as the improved p-n junction interface quality.

In the following discussions we will investigate the influences of the fabrication parameters such as the hole size and the doping conditions on the solar cell performance. Also, we have investigated the fabrication of nanoholes in both the (111) and (100) orientation Si wafers. Our results indicated the crystal orientation may have important effects on reflectance of the device. This will in turn have a substantial impact on the overall efficiency of the device. In section 4.4.5 we will discuss the influence of system randomness on the solar cell performances. The detailed fabrication conditions and cell performance data are listed in Tables 4.1 and

4.2. The discussions of table 4.1 will be presented in sections 4.4.1 to 4.4.4, while the discussions of table 4.2 as improved results will be presented in sections 4.4.6.

Table 4.1 Fabrication Condition & Cells Performances of PVC basing on p-type Si(111) wafer

No.	Ag Thickness/ nm	Annealing Time/min	Doping N_2 flow/sccm	Diffusion Time/s	Jsc/mA/cm^2	Voc/V	FF%	Efficiency%
T3-250	3	10	250	600	3.03	0.20	23.56	0.14
T3-500	3	10	500	600	2.49	0.47	25.01	0.29
T5-250	5	10	250	600	0.15	0.01	0	
T5-500	5	10	500	600	7.12	0.45	24.78	0.80
T5-750	5	10	750	600	7.09	0.49	24.41	0.86
T5-1000-2	5	10	1000	600	10.69	0.51	21.62	1.18
T10-250	10	10	250	600	1.01	0.10	24.33	0.03
T10-500	10	10	500	600	13.6	0.45	20	1.2
T10-750	10	10	750	600	9.84	0.49	23.59	1.14
T10-1000	10	10	1000	600	11.90	0.50	22.83	1.36
T15-250	15	10	250	600	8.345	0.19	24.43	0.39
T15-1000	15	10	1000	600	13.07	0.50	39.85	2.63

Table 4.2: Fabrication Condition & Cells Performances of PVC basing on p-type Si(100) wafer

No.	Ag Thickness/ nm	Annealing Time/min	Doping N_2 flow/sccm	Diffusion Time/s	Jsc/mA/cm^2	Voc/V	FF%	Efficiency%
P0T30-600	30	15	1000	600	6.79	0.48	26.26	0.86
P0T30-800	30	15	1000	800	11.43	0.50	35.72	1.99
P0T30-1000	30	15	1000	1000	13.35	0.49	45.91	3.01
P0T30-1200	30	15	1000	1200	11.84	0.49	54.89	3.18
P0T70-600	70	30	1000	600	0.82	0.47	22.05	0.09
P0T70-800	70	30	1000	800	1.47	0.54	17.67	0.14
P0T70-1000	70	30	1000	1000	16.95	0.49	32.94	2.63
P0T70-1200	70	30	1000	1200	14.17	0.45	41.54	2.5
P0T150-600	150	60	1000	600	15.73	0.56	26.81	2.31

P0T150-800	150	60	1000	800	13.22	0.49	29.16	1.89
P0T150-1200	150	60	1000	1200	13.89	0.49	26.97	1.83

4.4.1 The effects of nanohole size on cell performances

For better understanding of the data in table 4.1, figure 4.17 is used to illustrate the efficiencies of the all the cells fabricated with different silver film thickness and carrier gas flow rates, using Si (111) wafers.

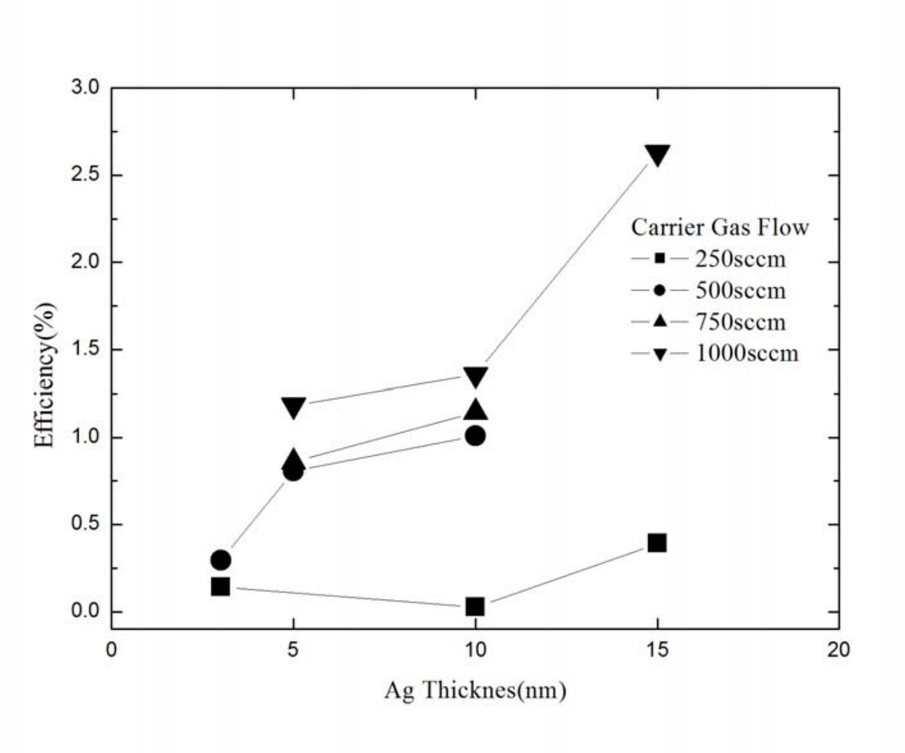

Figure 4.17: Efficiencies of nanohole solar cells based on p-type Si(111) fabricated from different Ag film thickness and with different carrier gas (N_2) flow rate.

From the results we observe that thicker Ag films yielded both larger average nanohole size and inter-hole distance, resulting in higher cell efficiencies. The improvement in the device performance is attributed to the relatively low doping concentration for the starting p-type wafer (10^{15} cm^{-3}) which requires a thicker a quasi-neutral region for the reduction of the series resistance of the device and to avoid the complete depletion of p-region of the silicon nanostructure. For example, the series resistances of devices fabricated from 10nm Ag and 15nm Ag are calculated from equation 2.37，the four PVCs made from 10nm Ag have *Rs*'s above 50 Ω cm^2 while the tow devices made from 15nm presents *Rs* below 25 Ω cm^2. 10nm Ag devices with smaller inter-hole distance demonstrate larger series resistances. This is important for the improvement of the *FF* of the device, figure 4.18 presents the I-V curves of the PVCs fabricated from 5nm, 10nm and 15nm Ag with 1000sccm carrier gas flow rate. Their series resistances are 93.8 Ω cm^2, 60.1 Ω cm^2 and 18.8 Ω cm^2 respectively. Our data demonstrate an inverse relationship between R_S and *FF*.

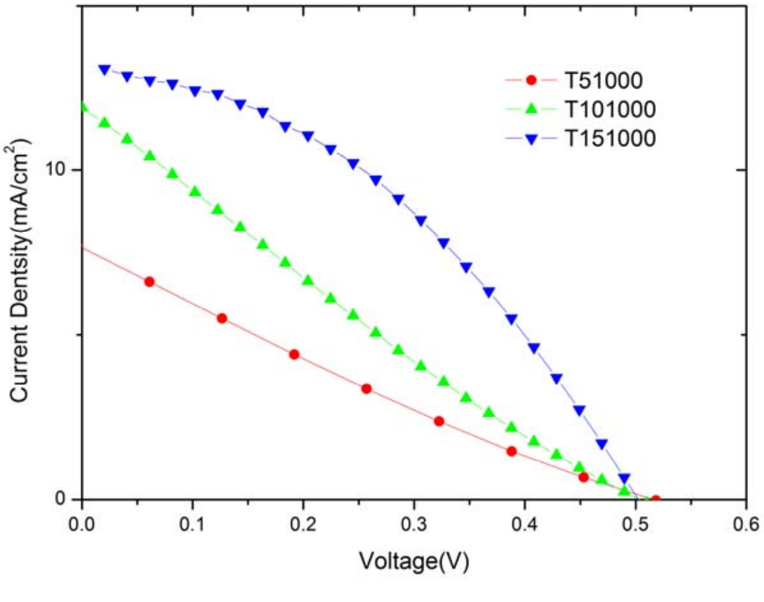

Figure 4.18: IV curves of PVCs fabricated from 5nm, 10nm and 15nm Ag with 1000sccm carrier gas flow rate (in sccm).

The results indicate that further improvement in the cell properties can be accomplished by optimizing the substrate doping concentration and the inter hole distance of the device, the improved results will be discussed in section 4.4.5.

4.4.2 The effects of doping conditions on cell performances

SIMS is used determine the doping concentration of the n-region, using planar wafer control sample. The doping concentration of the n-region is found to be 10^{20} cm^{-3}. Such high carrier concentration is consistent with the fact that no drive-in was performed in our fabrication process and, consequently, very high P concentration in the shallow n-type area is expected. It is believed that the SIMS analysis will provide a more accurate estimation of the carrier concentration than using the dark I-V characterization because of the high doping concentration of the device which will lead to high leakage current in the reverse bias condition.

In figure 4.17, as the doping depth increase the cell efficiency increases. Since the establishment of a low series resistance for the n-region is important for the improvement of the cell efficiency, deeper metallurgical junction results in lower resistance in the n-region therefore improvement in the cell efficiencies. The series resistances of PVCs made from 10 nm, and 15nm Ag on p-type Si(111) wafer, as well as 30nm and 70nm Ag on p-type Si(100) wafer were calculated from equation 2.37, shown in figure 4.19 (a) and (b).

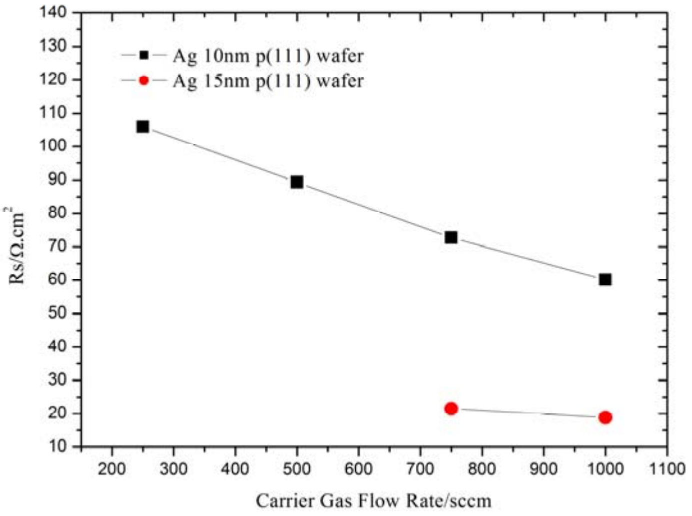

(a)

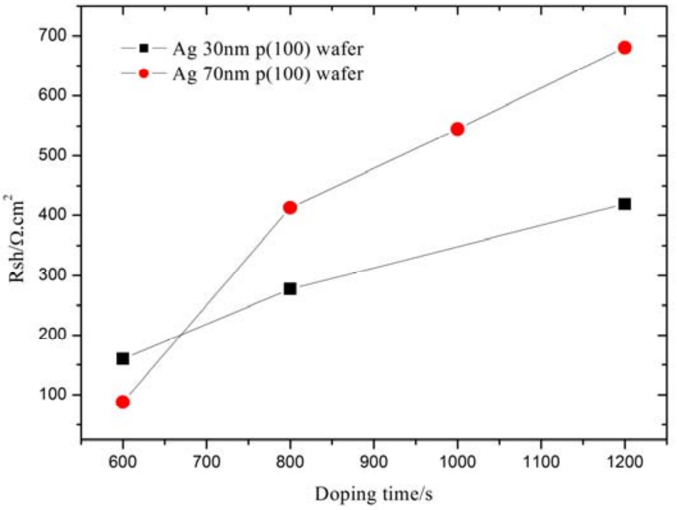

(b)

Figure 4.19: (a) Change of Serise resistance with doping carrier gas flow rate, PVCs fabricated from 15nm and 10nm Ag; (b) Change of Shunt resistance with doping time, PVCs fabricated from 30nm and 70nm Ag

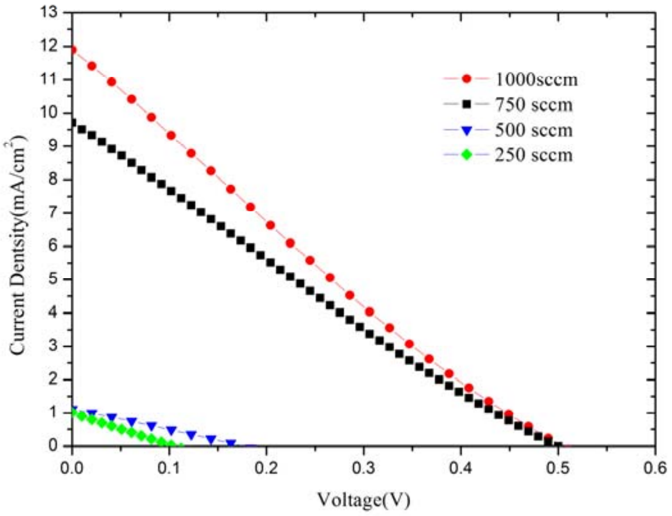

Figure 4.20: I-V curves of PVCs fabricated from 10nm and Ag with different carrier gas flow rate

The increasing of carrier gas flow and doping time resulted in the reduction of series resistance, as shown in figure 4.19(a). Figure 4.20 illustrates I-V curves of PVCs fabricated from 10nm and Ag with different carrier gas flow rate. For cells with deeper doping profile p-n junction depletion region can be shifted away from the surface and into the Si bulk region where the defects concentration is lower than that in the surface, therefore the recombination in the p-n junction depletion region can be reduced.

The existence of shunt resistance will result in the lowering of the cell efficiency by providing alternate current path [57] which results in the degradation in the *FF*. This is consistent with the observed improvement in the cell efficiencies with large carrier gas flow-rates and long doping times as shown in figure 4.19(b).

4.4.3 The influence front contact on cell performance

Figure 4.18 shows the solar cell cross-section with sputtered ITO covering upper part of the structure. The poor filling of the nanoholes by the sputtered ITO results in high series resistance of the device leading to poor *FF* for the PVCs. Thus, future improvement of the device will require the optimization of the doping profile as well as the conformal deposition of high quality transparent conductive oxide layer to facilitate effective collection of the electrons.

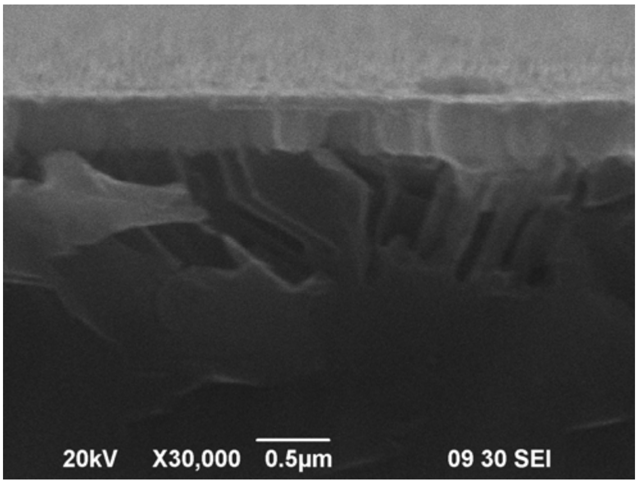

Figure 4.21: PVC cross-section with sputtered ITO covering upper part of the structure

4.4.4 The effects of Ag diffusion into the Si wafer

Silver, at high temperatures, will diffuse into silicon and form recombination centers. This reduces the carrier diffusion length and lower cells performances[58]. But in radial p-n junction solar cells, the carriers can be collected in a short distance horizontally, the influence of the reduction of carrier diffusion length on the cells performance can be mitigated. Other methods can also be used to prevent Ag diffusion into Si, for example it is believed using pulse laser annealing technique Ag diffusion will be significantly reduced. In such process the temperature on the Si surface is high enough for the formation of Ag islands, while the area below remains at low temperature, therefore preventing the diffusion of Ag into Si.

4.4.5 Reflectance

The reflectance spectra of a plane Si wafer and a nanohole-textured silicon wafer are shown in figure 4.20, which exhibit significant reduction compared to the plane wafer. The result is consistent with observations made by others[59]. This reduction in reflectance is attributed to light-trapping in the nano-hole structure[60].

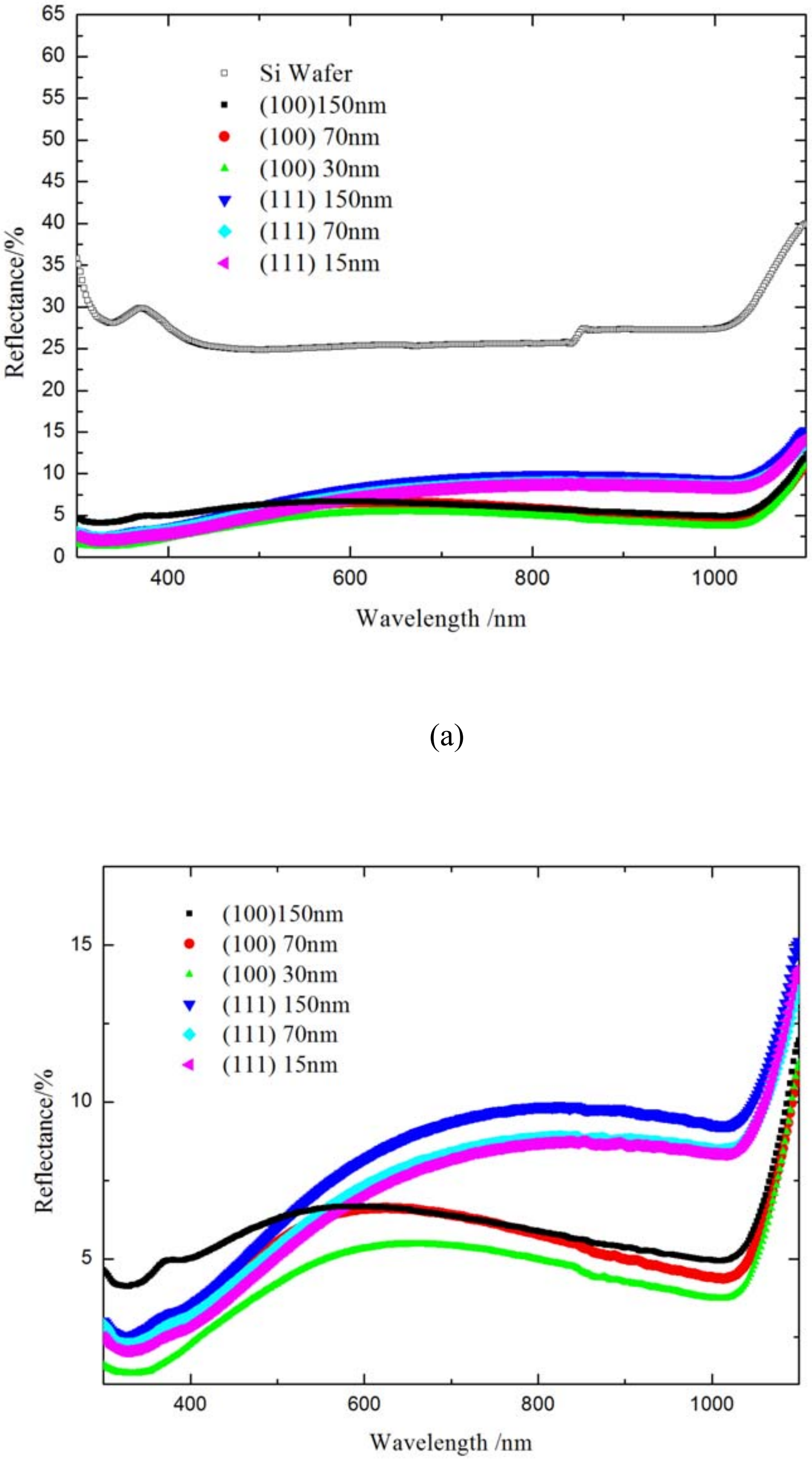

(a)

(b)

Figure 4.22: Reflectance of Si wafer with hole structure (a) With plane silicon wafer as control sample; (b) figure (a) in detail.

It can be observed that the reflectance curves can be divided into two groups: A(100) and B(111). Samples in (100) group with more vertical hole side wall present lower reflectance tan sample B. This result resembles that of vertical and slanting Si nonowires[61]. In each group, the reflectance decrease as the Ag film thickness or the hole size, indicating smaller structure dimension results in better light tapping.

4.4.6 Cells performances improvement

Figure 4.19 illustrates the efficiencies of the cells fabricated with different silver film thickness and carrier gas flow rates, using (100) wafer. It is important to note that while the cell efficiency increases initially with the thickness of the Ag film, upon further increase in the film thickness from 30 nm to 150 nm the cell efficiency is found to decrease. As to the influence of the junction depth, similar to previous analysis, as the doping time increase, which deepen the doping depth, the cell efficiency increase due to reduced resistance in n-region.

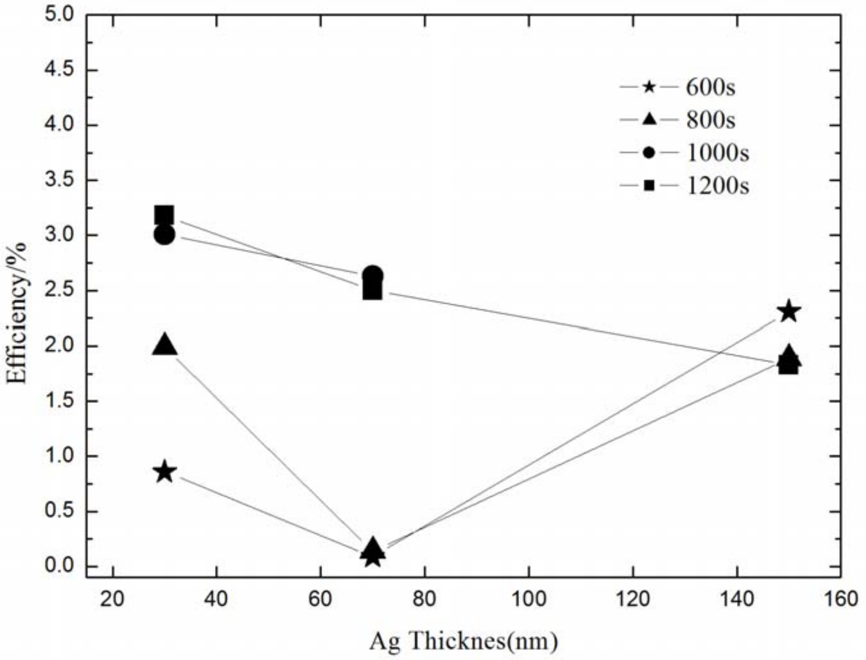

Figure 4.23: Efficiencies of nanohole solar cells based on p-type Si(100) wafer fabricated from different Ag film thickness and with different carrier gas (N_2) flow rate (the unit is sccm).

4.4.7 Influence of randomness structure

From the experimental results it is clear that while we have accomplished significant improvements compared to existing results from random nano-structure PVCs. However, η is still substantially below the ordered nano-structure PVCs. The random distribution of the nanohole size may partly explain the inferior performance of our cells compared to the highly ordered nano-structure PVCs. The complete device can be viewed as a collection of a large number of nanoscale PVCs with different sizes and optoelectronic properties and not all of them are in optimal conditions and thereby significantly affecting the overall cell performance.

5 Conclusion and Future Work

This project focuses on a simple and cost-effective technique to fabricate wafer-scale silicon nanohole radial p-n junction PVCs. By combining thermal annealing of Ag thin films and MCEE silicon nanoholes with controllable size, depth and distribution can be fabricated without using highly sophisticated equipment or processes. Moderate cell performances have been achieved, clearly demonstrating the potential of the technique in large scale fabrication of cost-effective nanostructure PVCs.

The morphology of self-formed Ag nano-islands by thermal annealing is investigated with systematic variations in the Ag film thickness, annealing time, annealing temperature, and silicon wafer surface property. The dimension of the islands can be effectively adjusted by changing Ag film thickness. In the RTA process, higher temperature (about 800℃) is more preferred to form islands with more round shape and uniform sizes. Sufficient annealing time is necessary to form Ag islands, and for thicker Ag films longer annealing time is required. If the Ag film is too thick, even after long annealing Ag islands can not form. The largest dimension for the Ag islands we obtained in the experiments is about several microns.

P-type Si wafers with both (100) and (111) orientation are used in the PVC fabrication. After MCEE the (100) wafers yields hole structures with more vertical side walls, and demonstrated lower reflectance, indicating better light trapping property. The PVC with best performance was based on (100) wafer.

To further lowering in the cost of the PVCs, we attempted to use Cu to as a catalyst for the electrochemical etching of Si in HF without the existence of H_2O_2, and Si hole patterns with 1um depth was successfully created, however the largest hole depth we can obtained is still not enough for PVCs fabrication.

In addition, we have conducted detailed investigations on the influences of the nanohole dimensions and doping conditions on the cell performances. As the hole sizes increase, the PVC efficiency increase at first, and then decrease while Ag film thickness > 30nm, this may be relevant to the balance of light trapping property and surface recombination. Larger doping depth usually leads to better performances due to the reduced resistance in n-type region.

Cells with poor *FF* and η may be ascribed to the poor filling of the nanoholes by the sputtered ITO that results in high series resistance. The random distribution of hole sizes may also partly explain the observed poor η of our cells comparing with cells fabricated with well ordered arrays.

For future improvement of the cell performance, interface passivation needs to be investigated to minimize surface recombination and to improve the cells performance.

To reduce the series resistance from the front contact, MOCVD ZnO is suggested to be used to form conformal front contact covering the whole surface structures.

Reference

1. Kazmerski, L. L. *Journal of Electron Spectroscopy and Related Phenomena* **2006,** 150, (2-3), 105-135.
2. Goetzberger, A.; Hebling, C.; Schock, H. W. *Materials Science & Engineering R-Reports* **2003,** 40, (1), 1-46.
3. Hoppe, H.; Sariciftci, N. S. *Journal of Materials Research* **2004,** 19, (7), 1924-1945.
4. Gratzel, M. *Journal of Photochemistry and Photobiology C-Photochemistry Reviews* **2003,** 4, (2), 145-153.
5. Landsberg, P. T.; Nussbaumer, H.; Willeke, G. *Journal of Applied Physics* **1993,** 74, (2), 1451-1452.
6. Luque, A.; Marti, A. *Progress in Photovoltaics* **2001,** 9, (2), 73-86.
7. Tian, B. Z.; Zheng, X. L.; Kempa, T. J.; Fang, Y.; Yu, N. F.; Yu, G. H.; Huang, J. L.; Lieber, C. M. *Nature* **2007,** 449, (7164), 885-U8.
8. Baxter, J. B.; Aydil, E. S. *Applied Physics Letters* **2005,** 86, (5), 3.
9. Arango, A. C.; Carter, S. A.; Brock, P. J. *Applied Physics Letters* **1999,** 74, (12), 1698-1700.
10. Gratzel, M. *Nature* **2001,** 414, (6861), 338-344.
11. Yang, P. D.; Yan, R. X.; Fardy, M. *Nano Letters* **2010,** 10, (5), 1529-1536.
12. Kayes, B. M.; Atwater, H. A.; Lewis, N. S. *Journal of Applied Physics* **2005,** 97, (11).
13. Um, H. D.; Jung, J. Y.; Li, X. P.; Jee, S. W.; Park, K. T.; Seo, H. S.; Moiz, S. A.; Lee, S. W.; Ji, J. Y.; Kim, C. T.; Hyun, M. S.; Park, Y. C.; Yang, J. M.; Lee, J. H.; Ieee, A novel photovoltaic nanodevice based on the co-integration of silicon micro and nanowires prepared by electroless etching with conformal plasma doping. In *2009 Ieee International Electron Devices Meeting*, Ieee: New York, 2009; pp 515-518.
14. Wang, X.; Peng, K. Q.; Wu, X. L.; Lee, S. T. *Electrochemistry Communications* **2010,** 12, (4), 509-512.
15. Tsakalakos, L.; Balch, J.; Fronheiser, J.; Korevaar, B. A.; Sulima, O.; Rand, J. *Applied Physics Letters* **2007,** 91, (23).
16. Tsakalakos, L.; Balch, J.; Fronheiser, J.; Shih, M. Y.; LeBoeuf, S. F.; Pietrzykowski, M.; Codella, P. J.; Korevaar, B. A.; Sulima, O.; Rand, J.; Davuluru, A.; Rapol, U. *Journal of Nanophotonics* **2007,** 1.
17. Garnett, E. C.; Yang, P. D. *Journal of the American Chemical Society* **2008,** 130, (29), 9224-+.
18. Garnett, E.; Yang, P. D. *Nano Letters* **2010,** 10, (3), 1082-1087.
19. Peng, K. Q.; Wang, X.; Li, L.; Wu, X. L.; Lee, S. T. *Journal of the American Chemical Society* **2010,** 132, (20), 6872-+.
20. Lu, Y. R.; Lal, A. *Nano Letters* **2010,** 10, (11), 4651-4656.
21. Kelzenberg, M. D.; Turner-Evans, D. B.; Putnam, M. C.; Boettcher, S. W.; Briggs, R. M.; Baek, J. Y.; Lewis, N. S.; Atwater, H. A. *Energy & Environmental Science* **2011,** 4, (3), 866-871.
22. Putnam, M. C.; Boettcher, S. W.; Kelzenberg, M. D.; Turner-Evans, D. B.; Spurgeon, J. M.; Warren, E. L.; Briggs, R. M.; Lewis, N. S.; Atwater, H. A. *Energy & Environmental Science* **2010,** 3, (8), 1037-1041.
23. Spurgeon, J. M.; Plass, K. E.; Kayes, B. M.; Brunschwig, B. S.; Atwater, H. A.; Lewis, N. S. *Applied Physics Letters* **2008,** 93, (3), 3.

24. Firat, E. FABRICATION AND CHARACTERIZATION OF SINGLE CRYSTALLINE SILICON SOLAR CELLS. MIDDLE EAST TECHNICAL UNIVERSITY, 2010.

25. Luque, A.; Hegedus, S., *Handbook of photovoltaic science and engineering*. J. Wiley: Chichester ; Hoboken, NJ, 2003; p xxvii, 1138 p.

26. Fonash, S. J., *Solar cell device physics*. 2nd ed.; Academic Press/Elsevier: Burlington, MA, 2010; p xxviii, 353 p.

27. Pierret, R. F., Advanced semiconductor fundamentals. In *Modular series on solid state devices v 6*, Addison-Wesley Pub. Co.,: Reading, Mass., 1987.

28. Lundstrom, M. S.; Schuelke, R. J. *Ieee Transactions on Electron Devices* **1983,** 30, (9), 1151-1159.

29. http://en.wikipedia.org/wiki/File:I-V_Curve_RS.PNG

30. http://en.wikipedia.org/wiki/File:I-V_Curve_RSH.PNG

31. Tsakalakos, L.; Balch, J.; Fronheiser, J.; Shih, M. Y.; LeBoeuf, S. F.; Pietrzykowski, M.; Codella, P. J.; Sulima, O.; Rand, J.; Kumar, A. D.; Korevaar, B. A.; Ieee, *Interaction of light with Si nanowire films*. 2006; p 111-113.

32. Burmeister, F.; Badowsky, W.; Braun, T.; Wieprich, S.; Boneberg, J.; Leiderer, P. *Applied Surface Science* **1999,** 144-45, 461-466.

33. Denkov, N. D.; Velev, O. D.; Kralchevsky, P. A.; Ivanov, I. B.; Yoshimura, H.; Nagayama, K. *Langmuir* **1992,** 8, (12), 3183-3190.

34. Hulteen, J. C.; Vanduyne, R. P. *Journal of Vacuum Science & Technology a-Vacuum Surfaces and Films* **1995,** 13, (3), 1553-1558.

35. Rybczynski, J.; Ebels, U.; Giersig, M. *Colloids and Surfaces a-Physicochemical and Engineering Aspects* **2003,** 219, (1-3), 1-6.

36. Hsu, C. M.; Connor, S. T.; Tang, M. X.; Cui, Y. *Applied Physics Letters* **2008,** 93, (13), 3.

37. Cheung, C. L.; Nikolic, R. J.; Reinhardt, C. E.; Wang, T. F. *Nanotechnology* **2006,** 17, (5), 1339-1343.

38. Peng, K. Q.; Xu, Y.; Wu, Y.; Yan, Y. J.; Lee, S. T.; Zhu, J. *Small* **2005,** 1, (11), 1062-1067.

39. Zhang, M. L.; Peng, K. Q.; Fan, X.; Jie, J. S.; Zhang, R. Q.; Lee, S. T.; Wong, N. B. *Journal of Physical Chemistry C* **2008,** 112, (12), 4444-4450.

40. Lin, L. H.; Guo, S. P.; Sun, X. Z.; Feng, J. Y.; Wang, Y. *Nanoscale Res Lett* **2010,** 5, (11), 1822-1828.

41. Peng, K. Q.; Zhang, M. L.; Lu, A. J.; Wong, N. B.; Zhang, R. Q.; Lee, S. T. *Applied Physics Letters* **2007,** 90, (16).

42. User:ARTE, Diagram of a scanning electron microscope. In Wikipedia, 2010.

43. http://en.wikipedia.org/wiki/File:PVeff(rev100921).jpg

44. Reinhardt, K. A.; Kern, W., *Hand Book of Silicon Wafer Cleaning Technology*. 2nd ed.; William Andrew Inc.: Lakewood, 2008.

45. Peng, K. Q.; Wang, X.; Li, L.; Wu, X. L.; Lee, S. T. *Journal of the American Chemical Society* **2010,** 132, (20), 6872-6873.

46. Peng, K. Q.; Wang, X.; Wu, X. L.; Lee, S. T. *Applied Physics Letters* **2009,** 95, (14), 143119.

47. Chern, W.; Hsu, K.; Chun, I. S.; de Azeredo, B. P.; Ahmed, N.; Kim, K. H.; Zuo, J. M.; Fang, N.; Ferreira, P.; Li, X. L. *Nano Letters* **2010,** 10, (5), 1582-1588.

48. Cai, W. P.; Zhong, H. C.; Zhang, L. D. *Journal of Applied Physics* **1998,** 83, (3), 1705-1710.

49. Zhao, Y. Q.; Leung, K. K.; Surya, C.; Feng, C. K.; Chen, Y. F.; Chen, D. M.; Shen, H.; Zhang, B. J.

In *Cost Effective Fabrication of Wafer Scale Nanoholes for Solar Cells Application.*, 2011 MRS Spring Meeting proceedings, 2011; 2011.

50. Huang, Z. P.; Geyer, N.; Liu, L. F.; Li, M. Y.; Zhong, P. *Nanotechnology* **2010,** 21, (46).

51. Pillai, S.; Catchpole, K. R.; Trupke, T.; Green, M. A. *Journal of Applied Physics* **2007,** 101, (9).

52. Krishna, H.; Sachan, R.; Strader, J.; Favazza, C.; Khenner, M.; Kalyanaraman, R. *Nanotechnology* **2010,** 21, (15), 155601

53. Tsakalakos, L.; Balch, J.; Fronheiser, J.; Korevaar, B. A.; Sulima, O.; Rand, J. *Applied Physics Letters* **2007,** 91, (23), 233117.

54. Garnett, E. C.; Yang, P. D. *Journal of the American Chemical Society* **2008,** 130, (29), 9224-9225.

55. Peng, K. Q.; Lee, S. T. - *Advanced Materials* **2011,** 23, (2), 198-215.

56. Jones, S. W., *http://www.icknowledge.com/misc_technology/Diffusion.pdf*. 2008.

57. http://pveducation.org/pvcdrom/solar-cell-operation/shunt-resistance.

58. Chen, L. H.; Zeng, Y. X.; Nyugen, P.; Alford, T. L. *Materials Chemistry and Physics* **2002,** 76, (3), 224-227.

59. Wang, F.; Yu, H. Y.; Wang, X. C.; Li, J. S.; Sun, X. W.; Yang, M. F.; Wong, S. M.; Zheng, H. Y. *Journal of Applied Physics* **2010,** 108, (2), 024301.

60. Han, S. E.; Chen, G. *Nano Letters* **2010,** 10, (3), 1012-1015.

61. Fang, H.; Li, X. D.; Song, S.; Xu, Y.; Zhu, J. *Nanotechnology* **2008,** 19, (25).